Effect of Vanadium on Grain Refinement of Aluminium

Audun Johanson

Summary

Today, grain refinement of aluminium is effectively achieved by inoculation. The performance of the inoculants, as well as further growth restriction in the liquid metal, can be affected by alloy- elements and impurities. A trend towards increasing amounts of some specific impurities in the coke- anode bring forth increasing amount of these elements in the final metal. One such element is vanadium. The effect of limited amounts of vanadium on the grain refinement is in this thesis assessed. Both the impact on inoculation properties and continued growth restriction is investigated. Levels ranging from 0 to 500 parts- per-million (PPM) is evaluated in a commercial 6060- aluminium alloy and highly pure 5N (99.999 % Al)- alloy. Thermal analysis and optical microscopy are used to investigate the solidification and final microstructure. Edge- to Edge Mismatch (E2EM)- model, Scanning Electron Microscopy (SEM), Focused Ion Beam (FIB) and Transmission Electron Microscopy (TEM) are applied to investigate the inoculants with respect to vanadium. Both theoretical and experimental evaluations indicate that vanadium has little or no effect on the grain refinement of aluminium at the investigated levels. Investigations of the inoculation particles also show that their composition and properties are unchanged. These results are consistent with the most recent literature.

Sammendrag

I dag oppnås kornforfining av aluminium effektivt ved hjelp av inoculanter. Egenskapene til inoculantene, samt videre vekst restriksjon i det flytende metallet, kan påvirkes av legerings- og spor elementer . En trend mot økende mengder av noen urenheter i koksanoden frembringer større andel av slike elementer i det ferdige metallet. Et slikt element er vanadium. Effekten av begrensede mengder vanadium på kornforfining av aluminium er i denne avhandlingen undersøkt. Både effekten på inoculerings egenskapene og påfølgende vekst restriksjon er undersøkt. Nivåer mellom 0 og 500 ppm er undersøkt både i en kommersiell 6060- aluminiums legering og i ren- 5N (99.999 % Al)- legering. Termiskanalyse og lys mikroskopi er benyttet til å undersøke størkningsforløpet og endelig mikrostruktur. Edge- to- Edge Mismatch (E2EM)- model, Scanning Electron Microscopy, Focused Ion Beam og Transmissions Elektron Mikroskopi er benyttet til å studere inoculant partiklene med hensyn på vanadium. Både teoretiske og eksperimentelle evalueringer indikerer at vanadium har liten eller ingen effekt på kornforfiningen av aluminium ved de undersøkte nivåer. Disse resultatene er konsistent med nyeste litteraturen om emnet.

Preface

The following work has been carried out at the Department of Materials Technology, Norwegian University of Science and Technology (NTNU), in cooperation with Alcoa Lista from January to June 2013.

Firstly, I want to thank my supervisors Associate Professor Marisa Di Sabatino Lundberg and co- supervisor Professor Lars Arnberg for their guidance and expertise. PhD Candidate Thomas Hartmut Ludwig has also been more than helpful with advising on most aspects of my work. I would also like to thank Liss Pedersen at Alcoa Lista for both providing the topic for my project, necessary materials and characterisation of my samples. Finally, I would also like to thank Dr. Yanyun Li at Sintef for help with TEM examination and Thomas Jäger at Vigeland Metal Refinery for supplying high purity aluminium.

Innhold

Tabeller

Figurer

Kapittel 1

Introduction

1.1 Aluminium

Aluminium alloys have been utilised for more than a century. Its combination of strength, low density, formability, corrosion resistance, conductivity and abundance makes the material ideal for a number of applications. Both the automotive and aerospace industry benefit greatly from the light weight and high strength of aluminium. Its conductivity and far lower density allows the material to compete with heavy and expensive copper to manufacture longer electrical conductors. Aluminium is also an great thermal conductor, making it highly applicable for heat transfer systems, including heat exchangers and cooling ribbons. Although primary aluminium production is highly energy consuming, the energy consumption during recirculation is only 5 % of that of primary production. Today, recirculation of post- consumer aluminium products saves over 90 million metric tones of CO_2 and over 100,000 GWh of electrical energy compared to primary production (Choate and Green, 2004).

1.2 Grain Refinement

The grain size of aluminium is greatly important both in terms of properties and manufacturing. The properties, including yield strength, ductility, hardness and conductivity all benefit from a smaller grain size. The relation between the grain size and several mechanical properties follow the The Hall- Petch relation:

$$\sigma = \sigma_0 + \frac{k}{\sqrt{D}} \tag{1.1}$$

Where σ_0 and k are material constants and D is the grain size. For large as- cast grain sizes, grain size strengthening is not apparent (Niels Hansen, 1977), and the above equation is not valid. However, the grain boundaries serves as sites for further recrystallisation and

are hence important in the following processing step. Grain refinement during casting of aluminium is beneficial for both Direct Chill (DC) casting of wrought alloys and shape casting of foundry alloys (McCartney, 1989b). The main goal is to suppress columnar growth and attain an equiaxed structure **(Fig. 1.1)**.
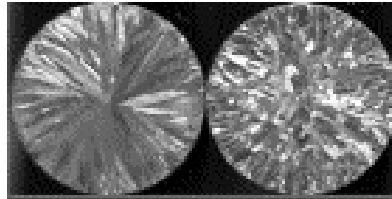
Figur 1.1: Cast structure of aluminium. The left structure is columnar with growth initiated from the crucible walls and directed according to the thermal gradient imposed through the same walls. For the right structure, the columnar growth is suppressed and a completely equiaxed structure is attained. (Wang et al., 2012a)

Equiaxed growth allows for little segregation and a uniform microstructure. This is essential for a positive and predictable response to subsequent post- cast treatments and the final mechanical properties (Granger, 1998). The uniformity of the structure is also critical during the casting itself. For DC casting, the alloys susceptibility to hot- tearing and cracking is greatly improved (Rooy, 1989). This allows for increased casting speed. An equiaxed structure will also improve feeding of liquid during casting, which reduces and disperses porosity. This is particularly important for shape casting. Grain refinement in aluminium can be achieved by a number of means. Today the most important path is by inoculation. By adding potent inoculation particles through a master alloy prior to casting, columnar growth is effectively suppressed. These master alloys rely on several mechanisms, where their exact composition and both intentional and un- intentional added solute elements may interfere. From a quality and cost perspective, utilising both the impurities and added alloy elements are necessary.

1.3   Impurities in Anodes

The anodes, utilized in the Hall- Heroult process for production of primary aluminium, are produced from petroleum coke. The coke is infested with the transition element vanadium which follows the anode into the electrolytic cells. Finally, some of the vanadium is found in the aluminium. The increase in aluminium production and hence carbon anode consumption is expected to increase the carbon costs. In turn cheaper alternatives with increasing impurity content makes its way to the aluminium products. Today, the aluminium industry experiences an increase of vanadium in the coke **(Fig. 1.2)**.
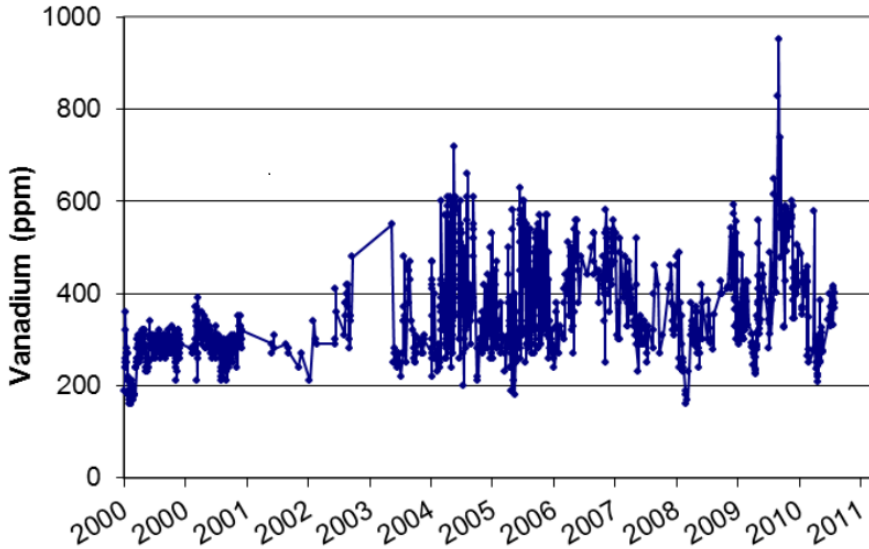
Figur 1.2: Change in vanadium for one US Golf Anode Coke (Edwards et al., 2012)

The increasing vanadium content in anode coke leads to increasing vanadium content in the molten aluminium. Established limits exist for most elements and operation within those should yield predictable products. However, as such limits are challenged and exceeded, investigation of the impact at these levels are crucial for accepting new limits. Positive or negative effects may require overall composition changes or costly refining steps to maintain the desired quality. Transition metals are usually removed by boron treatment, where boron is added to the melt to form borides that settle in the bottom (Cooper and Kearns, 1996). However, in terms of productivity and cost, such treatment should be limited, which consequently makes high vanadium tolerance desirable. One potential effect of increased vanadium is interference with the grain refinement.

1.4 Vanadium and grain size correlation

Alcoa Lista has recently found a correlation between increased vanadium levels and increased grain size. The importance of grain size and the tendency of dirtier carbon anodes, makes the relationship between those critical. In the present investigation, the impact of vanadium is assessed by a literature survey and experimental procedures which include thermal analysis, grain size measurements, and particle investigation by applying Scanning Electron Microscopy (SEM), Energy Dispersive Spectroscopy (EDS), Focused Ion Beam (FIB) and Transmission Electron Spectroscopy (TEM).

Kapittel 2

Theory

2.1 Structure development

The structure of aluminium evolves through several steps during its manufacturing process. Although a great deal of applied materials will go through post- casting treatments where flow and recrystallisation alter its microstructure, its as- cast structure is highly significant for its properties. Two basic solidification structures normally occur; columnar or equiaxed **(Fig. 2.1)**. The former is usually un- desirable during aluminium solidification. A fully equiaxed structure is necessary to achieve the optimal casting conditions and final properties. To suppress columnar growth is the main goal of grain refinement. Columnar growth is promoted by the heat extraction trough the crucible (or solid aluminium in the case of DC- casting). Solidification starts at the colder walls and continued growth occur in opposite direction of the heat extraction. Several methods exist too obstruct the columnar growth and obtain a fully equiaxed structure. These include stirring of the melt, inoculation, solid or semi- solid thermomechanical processing. For aluminium alloys, grain refinement of the as- cast structure is mainly achieved by inoculations. Inoculation eases the creation of new grains in front of the growing columns. The columns is blocked by equiaxed grains, resulting in a columnar- to equiaxed transition (CTE) (Wang and Beckmann, 1994). Creation of grains, both columnar and equiaxed are governed by two mechanism: nucleation and growth.

equiaxed zone

outer   inner

columnar zone
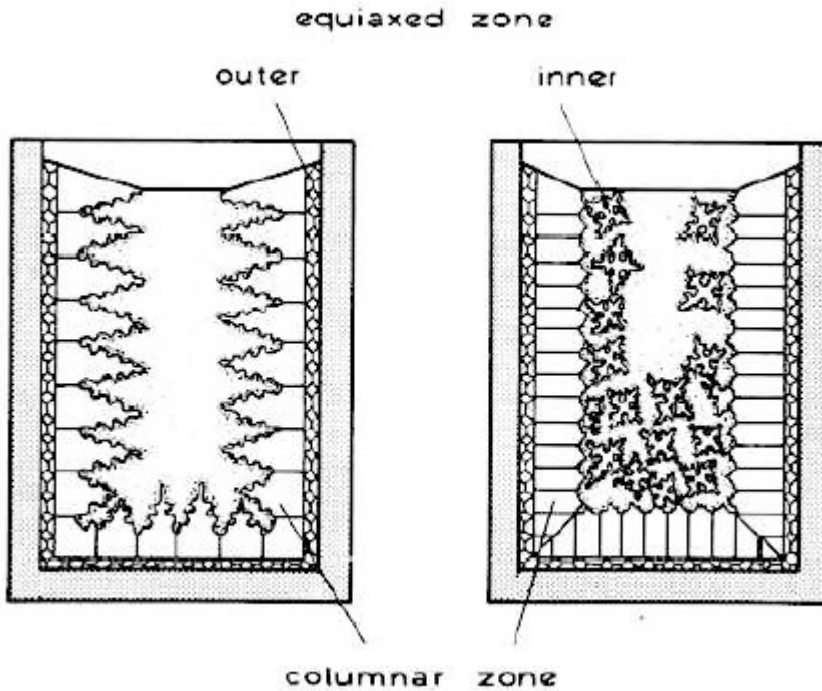
Figur 2.1: (Greer, 2011) Columnar growth starts from the crucible walls and results in one- directional elongated grains. A fully equiaxed structure can be achieved by effective grain refinement. Grain refinement rely on creation of grains ahead of the growing columnar grains. Such grains obstructs the columns and results in a transition from columnar- to equiaxed zone. Columnar- to- equiaxed transition (CET) is governed by alloy composition, pouring temperature, nuclei density in the melt, cooling capacity and melt convection (Wang and Beckmann, 1994)

2.1.1 Nucleation

The onset of transformation from one phase to another is termed nucleation. During solidification, the temperature in an melt is lowered. As the melting temperature of the melt is reached, a phase transformation from liquid to solid is favoured. However, this phase transformation will create an interface between the two phases. This interface will be associated with an interfacial energy proportional to the interface area. This is due to the excess atomic bonds at the crystal surface. The total energy change can be described by the following equation (Kurz, 1998):

$$\Delta G = V_\alpha \Delta G_{melt->\alpha} + A_\alpha \gamma_{\alpha/melt} \tag{2.1}$$

Where ΔG is the change in energy associated with solidification of a volume, V_α.

$\Delta G_{melt->\alpha}$ is the change in energy from the phase transformation itself. A_α and $\gamma_{\alpha/melt}$ are the interfacial- area and energy between the solidified material and the melt. **Fig. 2.2** illustrates **Eq. 2.1** for a nucleus. When ΔG starts to decrease with increasing size of nucleus, the nucleus is stable and it is energeticly favourable for it to grow. A critical size from which the nucleus is stable can thus be found from $\frac{d\Delta G}{dr} = 0$. ΔG at this size is ΔG^*. The nucleation rate is proportional to $exp[-\frac{\Delta G^*}{K_B T}]$, where K_B and T is the Boltzmann constant and temperature, respectively.
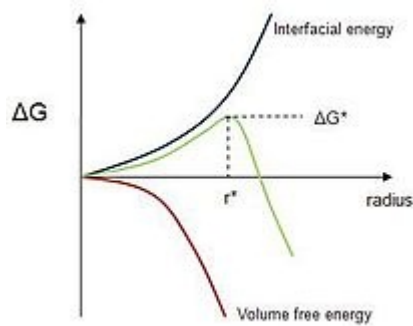
Figur 2.2: (Kurz, 1998) The figure illustrates **Eq. 2.1** for a nucleus. The total energy line constitutes of the volumetric energy term and the interfacial energy. For a sphere, the former is proportional with $radius^3$ and the latter with $radius^2$. When the derivative of the energy with respect to nucleus expansion becomes negative, growth of the nucleus is favourable. This basic description of nucleation is important for aluminium solidification and grain refinement as it can be related directly to the role of inoculation particles.

2.1.2 Heterogeneous nucleation

Nucleation may occur freely in the melt or on existing interfaces such as crucible walls or intentional or non- intentional particles in the melt. The former is termed homogeneous nucleation while the latter is termed heterogeneous nucleation. Homogeneous nucleation require considerable undercooling and is not relevant for aluminium solidification. Heterogeneous nucleation, on the other hand, significantly decreases the required undercooling. This is because the solidification on a surface will reduce the interface energy associated with that surface. The situation is often illustrated by a spherical cap in a flat surface. **Fig. 2.3** illustrates the spherical- cap model (Kurz, 1998).
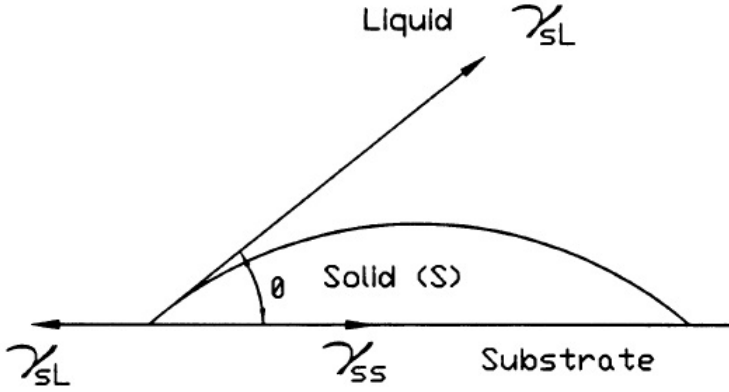
Figur 2.3: The drop- on- substrate system (Kashyap and Chandrashekar, 2001) illustrates the interface situation that arise during heterogeneous nucleation. The substrate- solid, substrate- liquid and solid- liquid interfaces are associated with different interfacial energies; $\gamma_{Substrate-solid}$, $\gamma_{solid-liquid}$, $\gamma_{substrate-liquids}$. To minimize energy an droplet with an wetting angle, ϕ is created. The same wetting angle dictate the effect of heterogeneous nucleation compared to homogeneous nucleation.

ΔG from (2.1) can now be multiplied with a function of the wetting angle, f(ϕ):

$$f(\phi) = \frac{2 - 3cos(\phi) + cos^3(\phi)}{4} \tag{2.2}$$

Eq. 2.2 dictates that nucleation can commence on low wetting angles and at a higher rate than on high wetting angle surfaces. This is effectively utilized during commercial grain refinement by adding inoculants. Inoculants are well- dispersed substrate particles, that are stable in the melt. Potent inoculants form a low wetting angle with the solidifying material. However, at low wetting angles, the model described above proves illogical. As the wetting angle falls below 10°, the nucleus is below one atom layer thick (Greer, 2011). At these cases, heterogeneous nucleation is better described by an atom- per- atom adsorption on the surface (Cantor, 2003; Kim and Cantor, 1994).

2.1.3   Crystal matching

The potency of inoculation particles relies on that the energy on newly formed interface must be lower than the surface energy associated with homogeneous nucleation. The interfacial energy of the interface between those depends on their crystal matching. A large difference will introduce a considerable strain and potential energy to the interface, in contrast to a similar structure, allowing for close- to relaxed, fully or partially coherent interface **(Fig. 2.4)**.
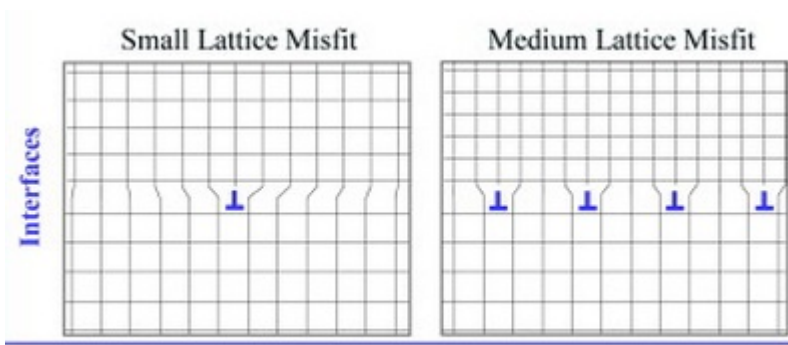
Figur 2.4: (Left) Little lattice strain for a small crystal mismatch between the lower substrate and upper solid crystal. (Right) Lattice strain due to larger mismatch between substrate and crystal (Meltzman et al., 2012). The same strain gives rise to potential energy which can be observed as larger wetting angle and in turn would require a larger driving force in order to nucleate the crystal.

A low interfacial interface requires two coherent or partially coherent phases, which have a certain orientation relationship (OR). The existence of an OR relies on a low discrepancy between atomic distances over the interface. Several models can predict inoculation properties based on the crystallographic discrepancy of the two phases. The simplest procedure only compares the interatomic spacing of two closed- packed planes. However, the interatomic spacing for different relative directions for the two phases, produces different interplanar distances between the atom rows. Edge- To- Edge Matching (E2EM) model minimizes both the interatomic mismatch in an closed-packed set of directions, and the corresponding interplanar mismatch between the line- ups of atom planes (Zhang et al., 2005). **Fig. 2.5** illustrates the basis for the E2EM model, where the edges of consecutive atom rows across an interface is the close- packed directions. The interatomic mismatch of the fully- or semi-coherent closed- packed directions is the most important, but in order to minimize strain energy over the interface, the stack of planes for the two phases should have similar interplanar spacing. The misfit threshold of the former is usually said to be 10 % to be considered an OR (Zhang et al., 2005). For the latter a mismatch of more than 6 % may force the phase to adjust its projected interplanar distance by rotating a few degrees and is considered as a threshold. The interatomic mismatch, f_r and interplanar mismatch, f_d over the semi- or -coherent interface is given by:

$$f_r = \frac{r_1 - r_2}{r_1} \tag{2.3}$$

And;

$$f_d = \frac{d_1 - d_2}{d_1} \tag{2.4}$$

Where r_1/d_1 and r_2/d_2 is the interatomic/ interplanar spacing for the two phases, 1 and 2, and the mismatch is calculated with respect to the former.
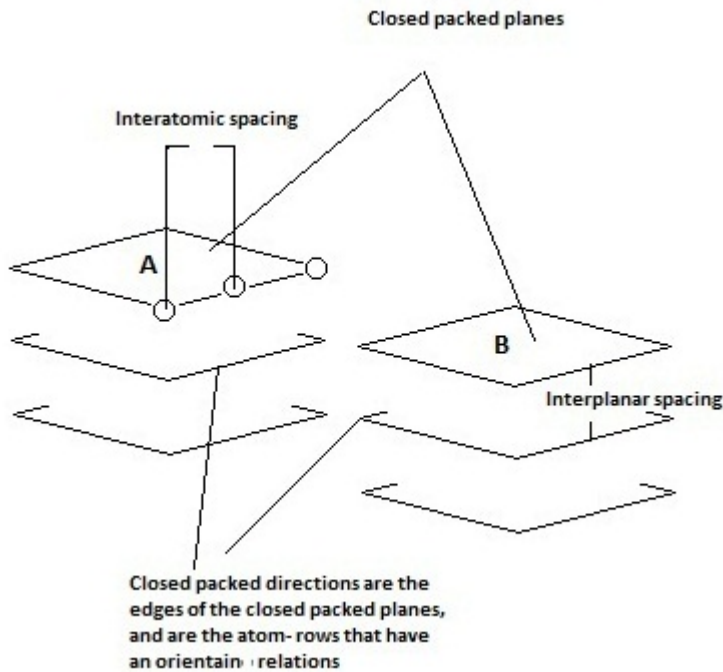
Figur 2.5: Edge- To Edge Mismatch (E2EM) Model evaluates both the interatomic mismatch over an interphases, and the interplanar mismatch of the consecutive atom rows. Edges of stacks of atom planes for two phases are the closed- packed directions which dictate the orientation relationship. Interatomic and interplanar spacing produces the two mismatch factors, f_r and f_d (Zhang et al., 2005).

2.1.4 Growth Restriction

Solidification is rarely an equilibrium process. As the liquidus temperature is reached, the system will strive towards a new assembly of equilibrium phases. This will require a re-distribution of solute. The change in equilibrium compositions are given by the liquidus slope, m_L and the partition coefficient, k **(Fig. 2.6)**, characterized by m and k (Kurz, 1998). Ruled by limited diffusion in the solidified matter, a pile- up or depletion layer ahead of the solid- liquid interface develops. This layer will have concentration gradient given by m, k and solute distribution in the liquid. The same concentration gradient is associated with a changing liquidus temperature **(Fig. 2.6)**. The resulting liquidus temperature gradient and the actual temperature gradient thus dictate the local undercooling **(Fig. 2.7)**. The liquid ahead of the solid- liquid interface is said to be constitutional undercooled when the temperature gradient is smaller than the liquidus temperature gradient **(Fig. 2.7)**. This will always be the case for equiaxed growth, where the crystals grow into an undercooled melt (in contrast to directional growth).
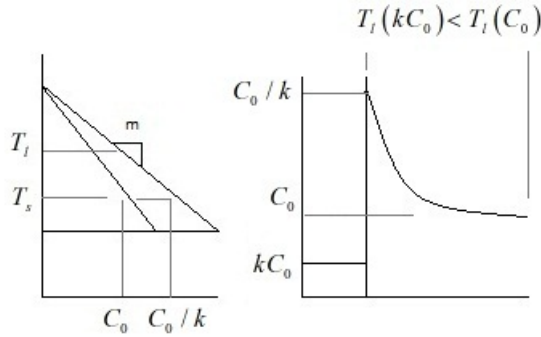
Figur 2.6: (Kurz, 1998) During the solidification process, the temperature is firstly lowered below the liquidus temperature, solidifying matter with a solute concentration given by kC_0. The continued solidification creates solid matter with solute concentration below the melt composition, C_0 until the solidus temperature is reached. Diffusion in solid is slow and does not allow for redistribution of solute to C_0. This means that the excess solute produced by lower- than- C_0 solidification is piled up at the moving solidification interface. From the solid- liquid interface, limited redistribution in the liquid produces a distribution boundary layer, where the concentration of solute decrease from $\frac{C_0}{k}$ to C_0. The change in solute concentration is associated with an changing liquidus temperature that increases from T($\frac{C_0}{k}$) to T(C_0). This change in liquidus temperature leads to the term constructionally undercooling, and is additive to the total undercooling.

The total undercooling is given by the temperature gradient and constitutional undercooling imposed by a solute gradient. In addition must the curvature of the solid- liquid interface and kinetic forces acting relative to the moving interface be taken into account. The total undercooling of the system, ΔT, is thus composed of the thermal component, ΔT_t kinetic component,ΔT_k,the curvature component,ΔT_c and the solute component,ΔT_s:

$$\Delta T = \Delta T_t + \Delta T_k + \Delta T_c + \Delta T_s \tag{2.5}$$

Of these components, only the undercooling due to solute can be controlled by alloy composition. The additional undercooling from solute will promote addition nucleation events adjacent to the initial nucleated grains (Qian et al., 2010; Quested et al., 2005; Easton and StJohn, 1999a; Quested and Greer, 2003). This will restrict the growth of the initial grain (**Fig. 2.7**).
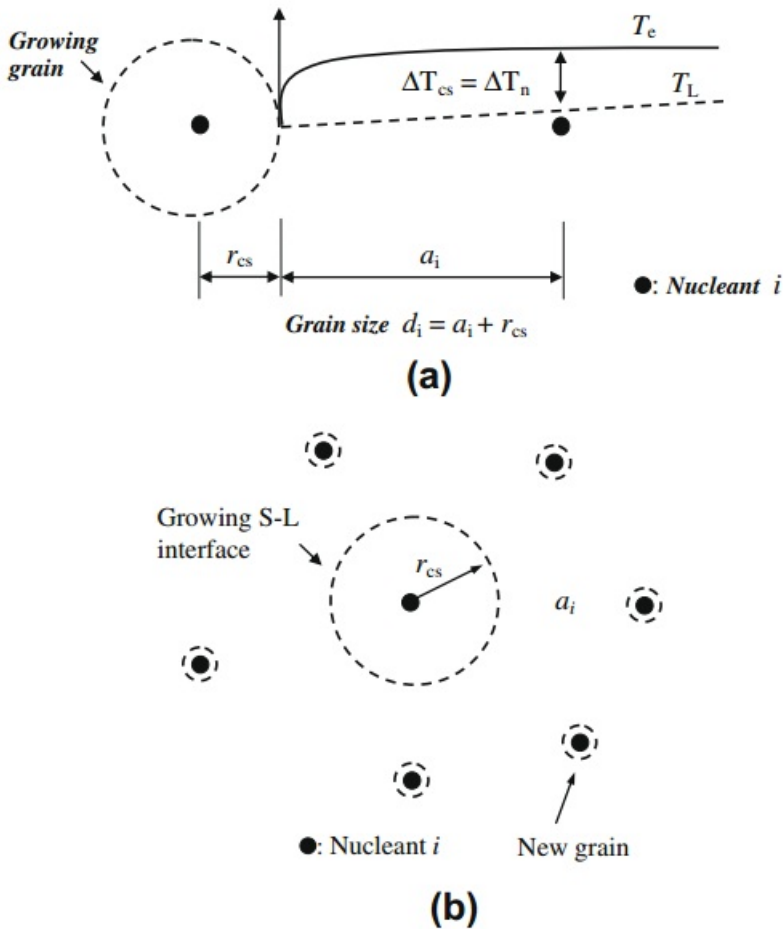
Figur 2.7: (a)The solute pile- up driven by the changing solidus concentration during the solidification process, and limited re- distribution in both solid and liquid, produces an distribution boundary layer. A constitutional undercooled region develops. The rate at which this region develops depends on the k and m values from the phase diagram of the actual system and the diffusivity of solute. These values thus quantify the growth restriction factor, GRF **Eq. 2.8**. (b) The undercooling activates neighbouring inoculants and restricts the growth (Qian et al., 2010).

The rate at which the constitutional undercooling develops in between grains correlates with the rate of nucleation and the final grain size (Easton and StJohn, 2001). If thermal diffusion is much higher than the solute diffusion, it would be the latter that limits the undercooling. This is the case if the growth of dendrites is fast enough. (Hunt, 1984; Rappaz and Thévoz, 1987; Chai et al., 1995) found the diffusion limited growth rate of dendrites to be:

$$V = \frac{AD(\Delta T)^2}{\Gamma m(1-k)c_0} \tag{2.6}$$

How fast the constitutional undercooling develops thus indicate how much the initial nucleated grains must grow before the undercooling becomes large enough to activate a neighbour inoculant. An relation between the developmental of constitutional undercooling and fraction solid is given by (Easton and StJohn, 2001):

$$\Delta T_c = mc_0(1 - \frac{1}{(1-f_s)^p}) \tag{2.7}$$

Where f_s is the fraction solid and p = 1-k. The initial rate, $\frac{d\Delta T_c}{df_s}$, can be found by differentiating when $f_s = 0$, giving:

$$\frac{d\Delta T_c}{df_s} = mc_0(k-1) \tag{2.8}$$

This equation tells us how fast the zone ahead of the solid- liquid interface becomes constitutional undercooled and is the growth restriction factor, GRF (Easton and StJohn, 2001; Quested et al., 2005). The contribution of different elements in a multi- component system can be summed to give the total GRF. The partition coefficient, k_i and liquidus slope, m_i for solute element i can be found from:

$$k_i = \frac{C_{S,i}}{C_{L,i}} \tag{2.9}$$

and

$$m_{L,i} = \frac{\partial T_L}{\partial C_{L,i}} \tag{2.10}$$

The m and k values calculated can then be used to find the individual GRFs for all solute elements and summed:

$$GRF_{total} = \sum_{i=1}^{n} m_{L,i}(k_i - 1)C_{0,i} \tag{2.11}$$

When the solute concentration is low, the individual GRFs has been suggested to be replaceable with their binary GRF- in other words: Neglect solute- solute interaction and consider the solution ideal (Quested et al., 2005). This is a very applicable approach as it removes the need for costly multi- component thermodynamic modelling to find the real k and m values.

2.2 Grain refining of Aluminium

The desired fine equiaxed structure in aluminium is effectively obtained by introducing inoculating particles by an master alloy. These refiners enhance the nucleation by both exploiting potent inoculants and growth restriction. The most common grain refiners are

today based on Al-Ti-B or Al-Ti-C. Al-Ti-B refiners are TiB_2 and Al_3Ti particles in an aluminium matrix. Both TiB_2 and Al_3Ti have been shown to be potent inoculants that share orientation relationships with aluminium **(Table. 2.1)**.

Tabell 2.1: Orientation Relationships between TiB_2/Al_3Ti and Aluminium

Interface	Plane	Direction	Reff.
Al_3Ti/Al	$(001)_{Al_3Ti}\|\|(012)_{Al}$ $(001)_{Al_3Ti}\|\|(010)_{Al}$ $(11\bar{2})_{Al_3Ti}\|\|(1\bar{1}\bar{1})_{Al}$	$[010]_{Al_3Ti}\|\|[010]_{Al}$ $[010]_{Al_3Ti}\|\|[010]_{Al}$ $[\bar{1}10]_{Al_3Ti}\|\|[01\bar{1}]_{Al}$	(Arnberg et al., 1982)
$(Al,Ti)B_2$/Al	$(20\bar{2}1)_{(Al,Ti)B_2}\|\|(311)_{Al}$ $(0001)_{(Al,Ti)B_2}\|\|(111)_{Al}$	na $[11\bar{2}0]_{(Al,Ti)B_2}\|\|[\bar{1}10]_{Al}$	(Zhang et al., 2005)

While TiB_2 is an efficient inoculants, the particle do require an limited undercooling to nucleate aluminium, which then again only occur on their basal plane. Al_3Ti removes the need for undercooling completely (Easton and StJohn, 1999b,a). The inoculation potency of Al_3Ti has been suggested to be enhanced by the peritectic reaction **(Fig. 2.8)**. Al_3Ti act as an precursors for aluminium that nucleates and envelopes the Al_3Ti- particle. The continued peritectic transformation of the particle require titanium to diffuse through the enveloping solid aluminium and the transformation is hence halted. Continued growth commence when the growth temperature is reached (Bäckerud et al., 1986).
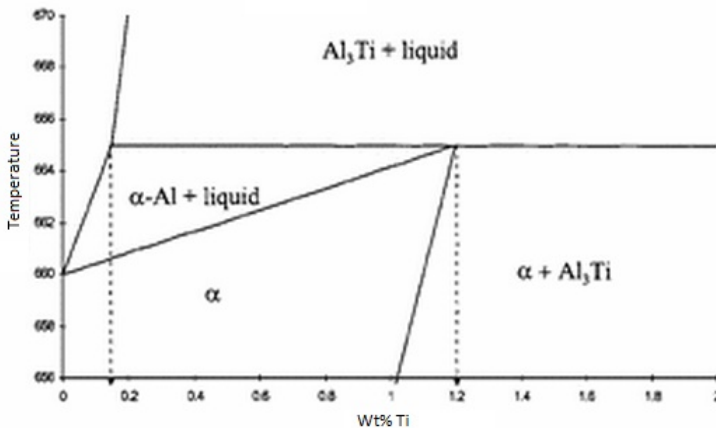
Figur 2.8: The aluminium rich part of the aluminium- titanium binary system. The peritectic reaction has been suggested to enhance the inoculation potency of the intermetallic Al_3Ti (Bäckerud et al., 1986). However, most compositions are far below the peritectic composition and Al_3Ti added by the grain refiner master alloy will dissolve.

Most compositions are hypo- peritectic. That means that Al_3Ti will dissolve. The apparent limited inoculation potency of TiB_2 and instability of Al_3Ti have lead to several suggestions for an combined mechanism. Three hypotheses are presented in **Fig. 2.9**.
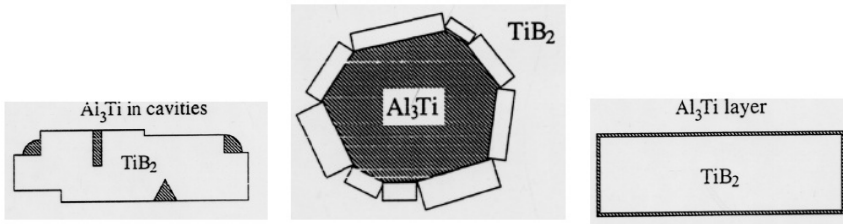
Figur 2.9: Three suggestion for the combined action of TiB_2 and Al_3Ti. TiB_2 is arguable not a good inoculant on its own. It is however, highly stable during the casting process. Al_3Ti will dissolve in most commercial solutions because the total titanium level is too low. This has lead to the above hypotheses. (Left) Cavities in TiB_2 preserve Al_3Ti (McCartney, 1989a). (Centre) A shell of stable TiB_2 preserves Al_3Ti (Bäckerud and Yidong, 1991). (Right) An adsorption layer of Al_3TI on the TiB_2 surface (Jones, 1985). The latter is supported by TEM- investigation of AlTiB- grain refiners added to a glassy aluminium precursor (Scumacher and Greer, 1994).

Of the three mechanisms proposed in **Fig. 2.9**, the adsorption model is best investigated and supported. By the use of a amorphous metallic glassy alloy and additions of AlTiB- grain refiner, study of nucleation and growth were possible (Scumacher and Greer, 1994). Under processing, the glassy matrix devitrificate to α-Al. An thin layer of Al_3Ti was adsorbed on the TiB_2 particles **(Fig. 2.10)**. The same layer took substantial time to dissolve (Schumacher and Greer, 1995). However, devitrification is much slower then real solidification and lacks convection. An similar study of nucleation and growth on TiB_2 in a real aluminium alloy is jet to be done.
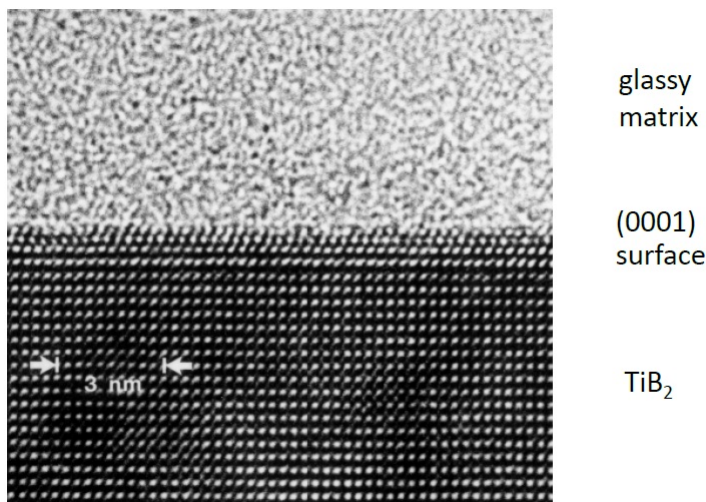
Figur 2.10: TEM investigation of TiB_2 in an aluminium glassy matrix reveal an coherent atom-layer that matches Al_3Ti (Greer, 2011).

Whatever the role of Al_3Ti, TiB_2 is ultimately responsible for nucleation. Of the

TiB_2 particles added only a small fraction act as a inoculant. The excess particles is pushed by the growing grains and end up along the grain boundaries. The in- active TiB_2 particles are mainly sub- micron particles, while the active inoculants are larger (Quested and Greer, 2004). This feature has been explained by the free growth model (Greer et al., 2000). Growth from an adsorbed layer is associated with a larger aspect ratio (area/volume) for a small particle compared to a larger one. Larger particles can therefore support growth at a smaller undercooling. As the undercooling increases, more and more inoculants are activated. However, when a certain nucleation rate is reached, the latent heat released from the grains surpass the heat extracted from the system. In turn the temperature increases and no more inoculants are activated. As most of the inoculants are small, most of the inoculants remains inactive and are found at the grain boundaries. Another issue regarding grain refinement is poisoning effects. Solute elements can interfere with the inoculants. Several elements is known to have detrimental effects on the inoculation performance. Zirconium is known to substitute titanium in TiB_2 (Bunn et al., 1999; Qiu et al., 2010) while silicon forms a layer of $TiSi_2$ on the TiB_2 particles (Quested et al., 2006) **(Fig. 2.11)**. The latter is handled by keeping the titanium level low, so that $TiSi_2$ do not form.
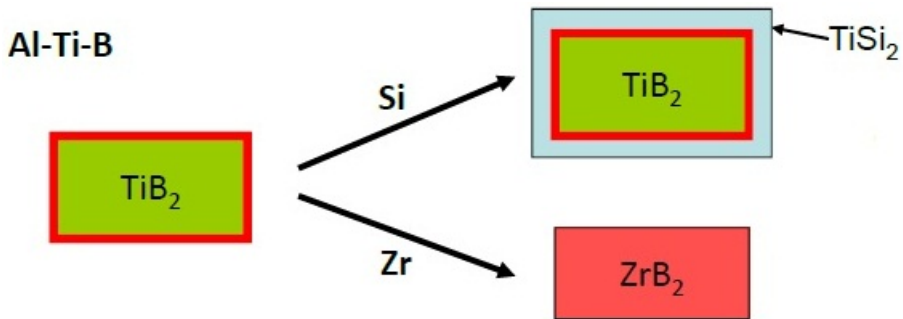
Figur 2.11: Poisoning mechanisms. Formation of an layer of $TiSi_2$ or bulk transformation by susbtituion of zirconium with titanium (Greer, 2011).

Grain refinement of aluminium also exploit the GRF. The Al-Ti-B master alloys must at least have a composition beyond stoichiometric TiB2. The master alloy will hence add excess titanium to the melt. This titanium may both be important according to a mechanism which include Al_3TI and the high GRF of titanium. **Table. 2.2** display the growth restriction for relevant elements in binary aluminium systems. As these factors are not additive, their individual effect varies from alloy to alloy. Solute- solute interaction can be detrimental for an elements individual contribution to GRF. (Dahle and Arnberg, 1997) found the grain size to increase with iron addition, while decreasing with magnesium addition. (Quested et al., 2005) explored the solute- solute interaction and its effect on the GRF. Such investigations show that a thermodynamic evaluation of any elemental additions is necessary, as it can have effects on the grain refiner performance.

Tabell 2.2: The growth restriction factor (GRF) for frequently faced binary systems (Easton and StJohn, 2001). The table suggest that particularly titanium has an considerable per- unit GRF. This is consistent with the requirement of excess of titanium in the molten aluminium. These GRF values are normally not additive and complex higher order thermodynamic evaluations are needed for reliable results. However, when the solute- solute interaction is weak or non- existent, the erroneous of additivity is small. (Quested et al., 2005)

Element	k_i	m_i	max. conc. (wt%)	m(k-1)	m(k-1) /k
Ti	7-8	33.3	0.15	~220	~30
Ta	2.5	70	0.10	105	42
V	4.0	10.0	~0.1	30.0	7.5
Hf	2.4	8.0	~0.5	11.2	4.7
Mo	2.5	5.0	~0.1	7.5	3.0
Zr	2.5	4.5	0.11	6.8	2.7
Nb	1.5	13.3	~0.15	6.6	4.4
Si	0.11	-6.6	~12.6	5.9	53.7
Cr	2.0	3.5	~0.4	3.5	1.8
Ni	0.007	-3.3	~6	3.3	4714
Mg	0.51	-6.2	~3.4	3.0	5.9
Fe	0.02	-3.0	~1.8	2.9	145
Cu	0.17	-3.4	33.2	2.8	16.5
Mn	0.94	-1.6	1.9	0.1	0.1

2.3 The effect of Vanadium

2.3.1 Literature on the effect of Vanadium

Until recently, the topic of the effect of vanadium on grain refinement has only been covered briefly in literature. Initially vanadium was thought to have a grain refining effect (Mondolfo, 1976). The effect was later confirmed, but at levels above 500 ppm (Abdel-Hamid, 1989). Below this level, the addition of vanadium had no effect in the presence of conventional grain refiners (Abdel-Hamid, 1989; Cook et al., 1997). Later on (Mahasneh and Al-Qawabah, 2011) found vanadium to increase the grain size in an Al- Cu alloy, while (Wang et al., 2012b) showed a significant grain refining effect above 1000 ppm, which was postulated to be due to the enabling of the peritectic reaction. However, the effect was independent of- and lower then for conventional grain refiners. (Grandfield et al., 2013; Jha et al., 2013) could no show any effect of vanadium on as- cast structure at values ranging from 100 ppm to 1100 ppm. (Wang et al., 2013) reviewed the effect above peritectic levels and found a considerable refining effect both due to growth restriction an formation of inoculation particles. Although somewhat inconsistent, the overall trend, with the exception of (Mahasneh and Al-Qawabah, 2011), is that vanadium has little or no effect at the levels that faces commercial aluminium manufacturing.

2.3.2 Effect on Inoculation

Diborides are found in a number of isomorph variants with different metals. Of these, the TiB_2 is the most stable (Khaliq et al., 2011). However, the less stable diboride, AlB_2, is also found in Ti- B- refined alloys (Zupanic, 2008). VB_2 is more stable than AlB_2 (Khaliq et al., 2011), and substitution of both titanium and aluminium with vanadium is possible. Al_3Ti can also be affected by the same mechanism, where the titanium is substituted for vanadium. **Fig. 2.12** show th Al- Ti- V ternary system at 873 K. The phase diagram show a continuous solid solution between Al_3Ti and Al_3V. Vanadium substitution of aluminium or titanium in both diborides or Al_3Ti may alter crystals. This might give rise to poisoning effects similar to the case of zirconium or silicon.

2.3.3 Effect on Growth restriction

From **Table. 2.2**, vanadium has a significant GRF in the binary aluminium system. This is understood from its binary phase diagram **(Fig. 2.13)**. A steep liquid line and large partitioning dictates a large segregation. Compared to titanium (Qian et al., 2010), vanadium is a slow diffuser (Murarka et al., 1968), which enforces the segregation.
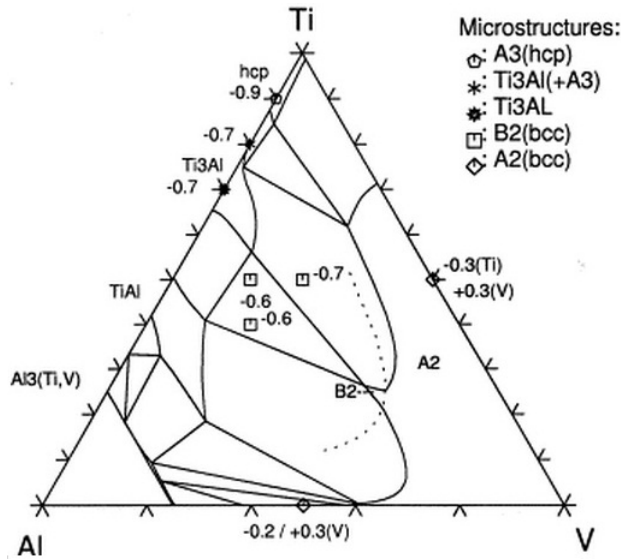
Figur 2.12: The isothermal section (873 K) of the Al-Ti-V ternary system (Diplas et al., 2002). A continuous solid solution is observed between Al_3Ti and Al_3V (Hayes, 1995).
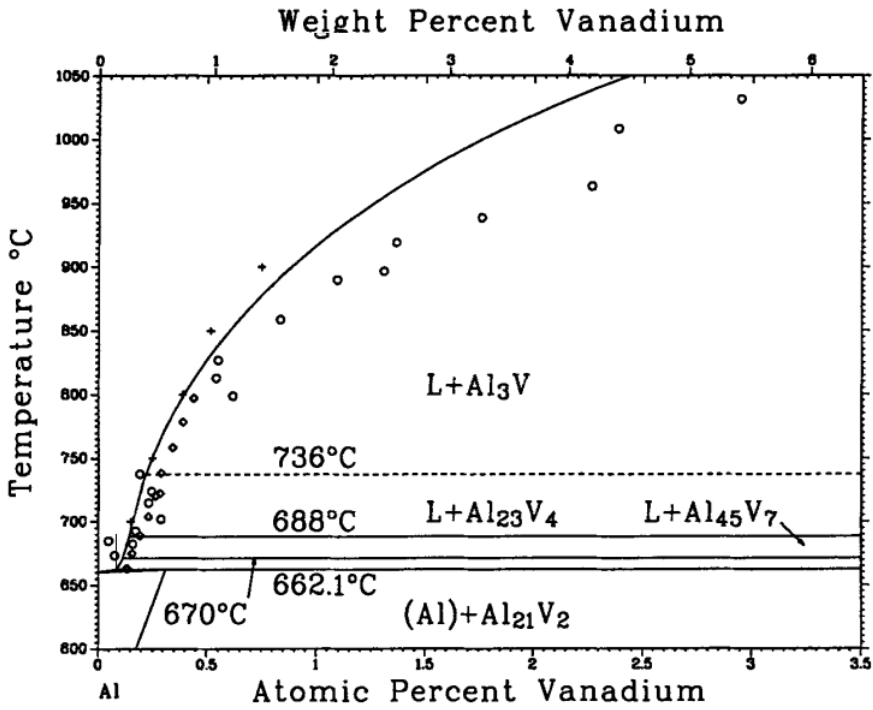
Figur 2.13: The Aluminium- Vanadium phase diagram (Murray, 1989).

Titanium will also be present in the solution and is the main contributor to the GRF. The combined GRF from titanium and vanadium depends on their interaction. (Quested et al., 2005) showed that in ternary alloys with solutes forming peritectic with aluminium- i.e. vanadium and titanium, the most important solute interaction is in α-Al. A positive regular- solution coefficient in α-Al increase the GRF (relative to non- interaction), while an negative regular- solution coefficient decrease the GRF. For the interaction in liquid aluminium, the effect is opposite. It was also shown that the size of the binary regular- solution coefficient between the two solutes correlates with the error in adding the binary GRFs **(Table. 2.2)**. Vanadium- titanium liquid alloys demonstrate a weak positive deviation from ideal behaviour (Kostov and Živković, 2008). Their solid regular solution coefficient is also positive, but larger than for the liquid (Murray, 1981). As the former is considered the most important of the two, it can be assumed that the interaction of titanium and vanadium increase the GRF. The small interaction also suggests that the error of simply adding the binary GRFs is small **(Table. 2.14)**.
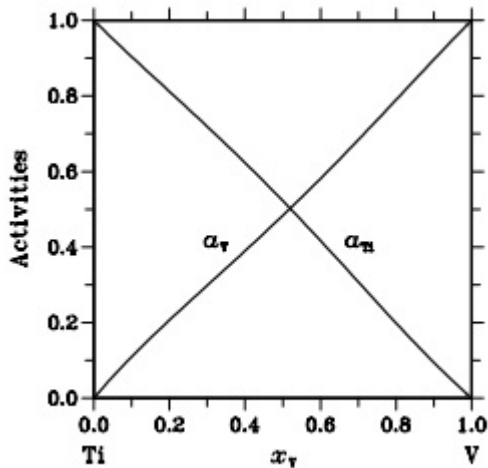
Figur 2.14: Activities of liquid titanium and vanadium in at 2200 K (Murray, 1981)

2.4   Thermal analysis

Thermal analysis offer an precise and practical approach to study the evolution of material structure during solidification. As solidification is provoked by extracting heat, latent heat due to fusion is produced. This brings about large observable changes in cooling behaviour. By measuring the temperature in the material throughout the solidification process, qualitative and quantitative aspects of the process can be revealed. In turn, such information can be related to the microstructure of the same material. **Fig. 2.15** displays the typical cooling- curve during an solidification process. Several characteristics events or sequences can be extracted from such curves:

- Basis cooling: Energy is extracted from the sample at a rate given by the thermal properties of the sample and its interaction with the surroundings.

- Nucleation: The onset of nucleation is associated with evolution of latent heat at a rate following from the nucleation rate and size of inoculates. In the case of effective inoculates and no associated nucleation resistance (free growth conditions), the nucleation temperature is expected to be the liquids temperature of the alloy.

- Supercooling: The nucleation rate and hence latent heat evolution are inversely proportional to supercooling. Accelerated heat release following from the external heat extraction halts the cooling of the melt at a maximum supercooling and following recalescence commence.

- Recalescence: As cooling continues, increasing growth rate and accelerated latent heat release surpass the external heat extraction and the melt will increase in temperature.

- Growth: Recalescence increase the temperature and halts continued nucleation. Now will only free growth of already nucleated grains produce heat, which equals the externally extracted heat. The temperature is thus kept constant through the growth phase.
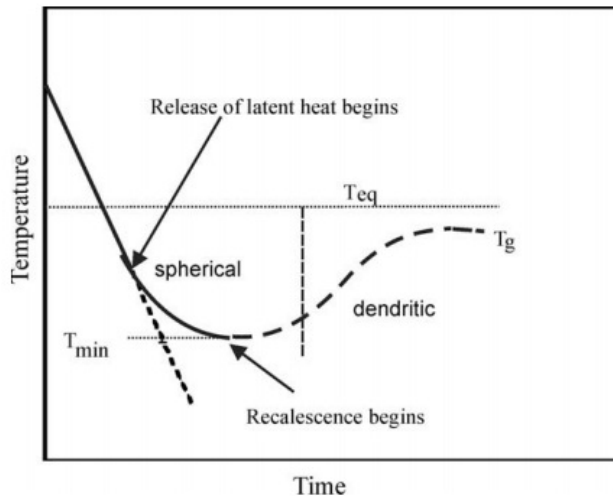
Figur 2.15: A typical thermal analysis and characteristic temperatures (Wang et al., 2012a). T_n indicate the temperature at which nucleation starts. This temperature depends on the required nucleation driving force. An effective inoculation or substrate particle may reduce this to close to zero and T_n is then equal to the liquidus temperature. T_{min} is the recalescence temperature where the nucleation rate evolve more latent heat than heat removed from the system. Thus will the nucleation rate decrease and less heat is evolved until nucleation stops at the growth temperature T_g. The latent heat produced by growth equals the heat removed by the system. Thus a temperature plateau is seen until the solidification reaction is completed and the temperature continue to decrease.

While the recalescence and growth temperature is easily found by the minimum and subsequent maximum temperature, respectively, the nucleation temperature is more difficult to accurately identify. In order to identify nucleation events, the temperature change must be isolated from the impact of latent heat release. This normal- cooling rate is a function of temperature. The cooling- rate as a function of temperature that is valid when no latent heat is released is called an baseline- function, dT(T). An baseline is created by evaluating the region of the cooling curve where no phase transformation occur $(T_{liq} < T < T_{sol})$. A polynomial of an desired accuracy/order is created from this region. The resulting baseline function is compared to the real cooling rate. Any deviation between those curves signify that the cooling is disrupted by evolution of latent heat and any nucleation temperature can be pinpointed.

3

Kapittel

Experimental Work

A experimental study of the impact of vanadium on the grain refinement of aluminium was conducted by the means of thermal analysis, grain size measurement, diboride particle investigation and the theoretical E2EM- model. Two basis materials were used; a 5N-quality (99.999 $wt\%$) aluminium alloy and a 6060 commercial alloy. The two basis materials were subject to controlled additions of vanadium and commercial Al-5Ti-B grain refiners ($5wt\%Ti$ and $1 \ wt\%B$). The samples were solidified at two different cooling rates, 1.25^oC/s and 4.0^oC/s.

3.1   Material Composition, Quality and Preparation

Three different vanadium additions were investigated. Meanwhile the titanium and boron addition were kept constant. One of the samples were subject to doubled titanium and boron addition without vanadium addition. **Table. 3.1** show the sample designation, basis material, vanadium-, titanium-, and boron- additions and cooling rate.

Tabell 3.1: Sample designation, composition and cooling- rate

Sample nr.	Basis Material	Vanadium [PPM]	Titanium [PPM]	Boron [PPM]	Cooling rate [^oC/s]
S1	5N-Al	0	30	6	1.25
S2	5N-Al	75	30	6	1.25
S3	5N-Al	500	30	6	1.25
CS1	6060	0	30	6	1.25
CS2	6060	75	30	6	1.25
CS3	6060	500	30	6	1.25
CS4	6060	0	60	12	1.25
CS5	6060	0	30	6	4.0
CS6	6060	500	30	6	4.0

The actual compositions of the 6060- samples after casting was measured by Opti-

cal Emission Spectroscopy (OES) **(Appendix. 7.4)**. Glow Discharge Mass Spectroscopy (GDMS) was used to measure the composition of the 5N- samples after casting **(Appendix. 7.5)**. The 5N- and 6060- basis pre- cast material composition is given in **Appendix. 7.1 and 7.2**. The basis material was squared by an discotome and cleaned by coarse grinding before treatment in ultrasound bath. The 5N- Al was macro etched in 17% HCl for 24 hours. A commercial 10% Vanadium master alloy was diluted with 5N- Al to 0.5%. This was done in order to improve the homogeneity of the master alloy and make small vanadium additions more convenient. For boron and titanium additions, a commercial Al-5Ti-1B master alloy rod was used. The composition of the rod is given in **Appendix. 7.3**.

3.2 Casting set- up and Thermocouples

Two different cooling rates were applied. The lower rate was achieved by free cooling of the crucible in air with the top covered by fibrefrax. The faster cooling rate was achieved by pressurized air flow. The resulting cooling rates were approximately 1.25 and 4.0 ^oC/s **(Appendix. 7.6)**. Thermal data was logged at 50 Hz with a Cambell data logger. Two k-type thermocouples coated with boron nitride (BN) was used. The thermocouples is re-coated between usage. Thermocouples is associated various forms of instability, regarding their measured temperature. This is usually seen as an initial transient before stabilisation. The stable temperature is not necessary exact, but often to high or low. The thermocouples were therefore calibrated against 5N- Al with a reference melting temperature of 660.3 ^oC. Calibration was repeated until stabilisation. In time, high temperature and work of the metal in the thermocouples change their properties slightly which in turn can cause drift of the read temperature. The thermocouples are thus re- calibrated in between the experiments. The thermocouples were initially interchanged between every analysis, but one showed significant instability during its drift- check after the 4'th sample. This thermocouple and the analysis performed with this thermocouple before this drift- check were thus rejected.

3.2.1 Procedure

Approximately 1 kg- batch of each alloy was melted in an clay graphite crucible. The crucible was coated with fibrefrax and BN. The sample was heated to 750 ^oC. The temperature in the melt was controlled frequently with a thermocouple. Oxide skimming was performed before and after every interaction with the melt. When the melt temperature reached 750 ^oC, the V- master alloy was added with subsequent stirring. The V- master alloy was given 30 min to dissolve before the Al-5Ti-B- master alloy was added with subsequent stirring. The Al-5Ti-B- master alloy was given 15 min to dissolve. Graphite crucibles (outer diameter 50 mm, height 50 mm, wall thickness 10 mm) were used to extract melt from the larger crucible. The small crucibles were pre- heated to 750^oC and floated on top of the melt for 1 min before they were dipped into the melt to extract a sample. The crucibles were placed in the thermal analysis set- up and the temperatures were logged. The melt was stirred between the analyses. Every sample extraction was performed between 730 - 740^oC. In total 6 parallel samples were extracted for each composition,

where 4 samples were used for thermal analysis, 1 sample was dedicated for grain size measurements and 1 sample was extracted for element analysis.

3.2.2 Thermal Analysis

The extracted data were smoothed and normalized to the point of maximum curvature (minimum temperature). This points serves as an common reference point for creation of an average curve for each composition. The characteristic nucleation-, recalescence-, undercooling and growth- temperature for each parallel samples was estimated before average over each composition. The nucleation temperature was estimated by creation of a baseline, while recalescence and growth temperature are determined from maximum and minimum curvature, respectively **(Fig. 3.1)**.
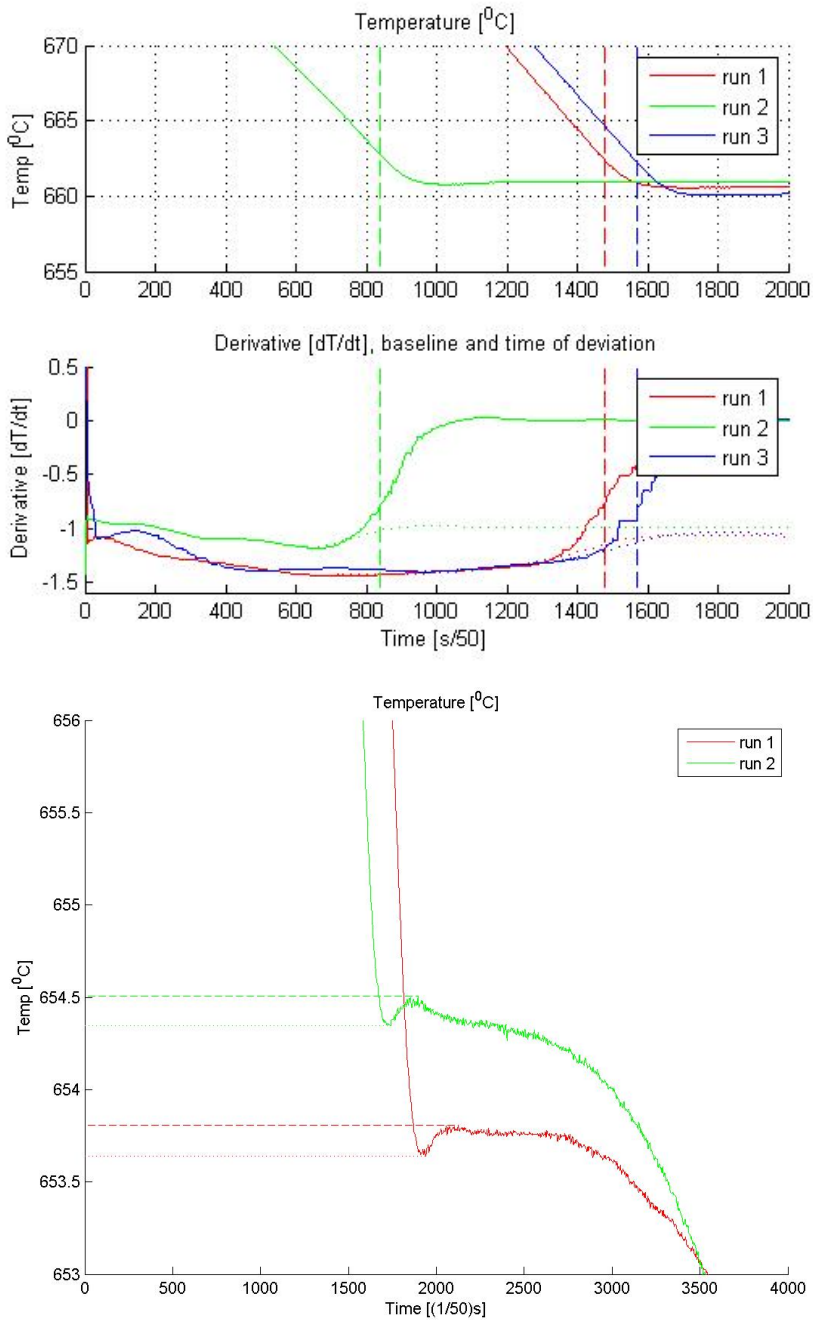
Figur 3.1: (Upper) Nucleation temperature determined from baseline - derivative deviation. (Lower) Recalescence and growth temperature found from maximum and minimum curvature. The undercooling is the growth - recalescence temperature difference.

3.2.3 Grain size measurements

For measurement of the grains size, selected samples were cut 1 cm above the bottom, ground and polished down to 1 μm. The 6060- samples were anodized in an HBF_4 solution, while the 5N samples were macro etched in an NaOH solution. Mean lineal intercept method under polarized light was used to measure the grain size of the 6060- samples. Two parallel samples for each composition were investigated. Four frames of 13.5 mm^2 for each sample were measured by a 5 X 5 grid, where each interception with an grain boundary was counted. Thus a total area of 8 X 13.5 mm^2 was measured for each composition. This yields 800- 1000 intersections. In addition was line- intersection method used in- scope to confirm the results. (In- scope observations both cover a larger area and lets the operator change the polarisation to reveal all grain boundaries, which were not possible to capture in a single photograph). The grain size of the 5N- samples were qualitatively rated.

3.3 Particle Analysis

3.3.1 Scanning Electron Microscopy

Borides with or without vanadium were assumed to be found mainly at the grain boundaries together with other segregated particles. The borides responsible for nucleation can be found at the grain centres. While the former type was expected to consist of single- or clusters of borides, too small to act as effective inoculants, the latter is assumed to be larger (Quested and Greer, 2004). An Hitachi scanning electron microscopy (SEM) W/ Backscatter detector (BEI) and Energy- dispersive X-ray Spectroscopy (EDS) was applied to find borides and investigate the infiltration of vanadium for the low and high vanadium-samples respectively.

3.3.2 Focused Ion Beam and Transmission Electron Microscopy

Transmission Electron Microscopy (TEM) offer a superior EDS resolution due to the small emission volume of thin samples. TEM also provide both crystal lattice and matrix matching information. An Helios NanoLab DualBeam Focused Ion Beam(FIB)/SEM was used to isolate and extract borides for an TEM sample. The preprepared TEM- sample was investigated in a Jeol TEM with respect to vanadium.

3.3.3 Edge- To- Edge- Mismatch- Model

Substitution of titanium or aluminium for vanadium in either diborides or Al_3Ti will change the crystal characteristics and may hence alter the inoculation properties for better or worse. The E2EM- model was used to evaluate the change in crystal matching and whether a poisoning effect is likely to happen from a crystallographic point of view. The crystal structures of the three phases, MB_2, Al_3M and aluminium, are listed in **Table. 3.2**, together with the calculated closed- packed rows and closed packed planes. M signify either aluminium, titanium or vanadium. The E2EM- model apply the interatomic spacing, r_{uvw} and interplanar spacing, d_{hkl}, which are found along the closed packed rows and between

the closed packed planes. The crystallographic data listed in **Table. 3.2** was used to calculate the interatomic mismatch, f_r and interplanar mismatch, f_d between the the possible orientations of the different phases.

Tabell 3.2: Crystal parameter of aluminium, MB_2 and Al_3M, where M signify aluminium, titanium or vanadium.

Phase	Structure	Lattice Par. (nm)			CP Direction	r_{uvw}(nm)	CP Plane	d_{hkl}(nm)
		a	b	c				
					(Zhang et al., 2005)			
Al	Cubic	0.4049	-	-	$\langle 110 \rangle^S$	0.2863	$\{111\}$	0.2338
					$\langle 100 \rangle^S$		$\{200\}$	0.2025
					$\langle 112 \rangle^S$		$\{220\}$	0.2025
					(Boulechfar et al., 2010)			
Al_3Ti	Tetragonal	0.3844	-	0.8623	$\langle 201 \rangle^S$	0.1880	$\{112\}$	0.2301
					$\langle 110 \rangle^S$	0.2725	$\{004\}$	0.2146
					$\langle 100 \rangle^S$	0.3854	$\{200\}$	0.1927
Al_3V	Tetragonal	0.3768	-	0.8313	$\langle 201 \rangle^S$	0.1843	$\{112\}$	0.2249
					$\langle 110 \rangle^S$	0.2673	$\{004\}$	0.2080
					$\langle 100 \rangle^S$	0.3780	$\{200\}$	0.1890
$Al_3Ti_{0.5}V_{0.5}$	Tetragonal	0.3809	-	0.8470	$\langle 201 \rangle^S$	0.1843	$\{112\}$	0.2249
					$\langle 110 \rangle^S$	0.2673	$\{004\}$	0.2080
					$\langle 100 \rangle^S$	0.3780	$\{200\}$	0.1890
					(Zhang et al., 2005)			
TiB_2	Hexagonal	0.3038	-	0.3239	$\langle 11\bar{2}0 \rangle^S$	0.1519	$\{0001\}$	0.3239
					$\langle 0001 \rangle^S$	0.3239	$\{0\bar{1}10\}$	0.2631
					$\langle \bar{1}\bar{1}23 \rangle^S$	0.0880	$\{0\bar{1}11\}$	0.2042
					$\langle 10\bar{1}0 \rangle^S$	0.2631	$\{11\bar{2}0\}$	0.1519
AlB_2	Hexagonal	0.3009	-	0.3262	$\langle 11\bar{2}0 \rangle^S$	0.1505	$\{0001\}$	0.3262
					$\langle 0001 \rangle^S$	0.3262	$\{0\bar{1}10\}$	0.2606
					$\langle \bar{1}\bar{1}23 \rangle^S$	0.0881	$\{0\bar{1}11\}$	0.2036
					$\langle 10\bar{1}0 \rangle^S$	0.2606	$\{11\bar{2}0\}$	0.1505
					(Predel, 1992)			
VB_2	Hexagonal	0.2998	-	0.3056	$\langle 11\bar{2}0 \rangle^S$	0.1499	$\{0001\}$	0.3056
					$\langle 0001 \rangle^S$	0.3056	$\{0\bar{1}10\}$	0.2596
					$\langle \bar{1}\bar{1}23 \rangle^S$	0.0843	$\{0\bar{1}11\}$	0.1979
					$\langle 10\bar{1}0 \rangle^S$	0.2596	$\{11\bar{2}0\}$	0.1499

Kapittel 4

Results

4.1   5N Aluminium

4.1.1   Thermal Analysis of 5N - Alloy

The temperature - time curves measured were smoothed and average curves were constructed relative to the point of maximum curvature (recalescence temperature). A high resolution portion of the resulting curves for the different vanadium compositions is displayed in **Fig. 4.1**. The temperature- time curve from one of the thermal analysis of S-3 was clearly corrupted and hence discarded. The average curve for Sample S-3 was thus constructed from only three measurements. The complete collection of thermal analysis is provided in **Appendix. 7.7**.
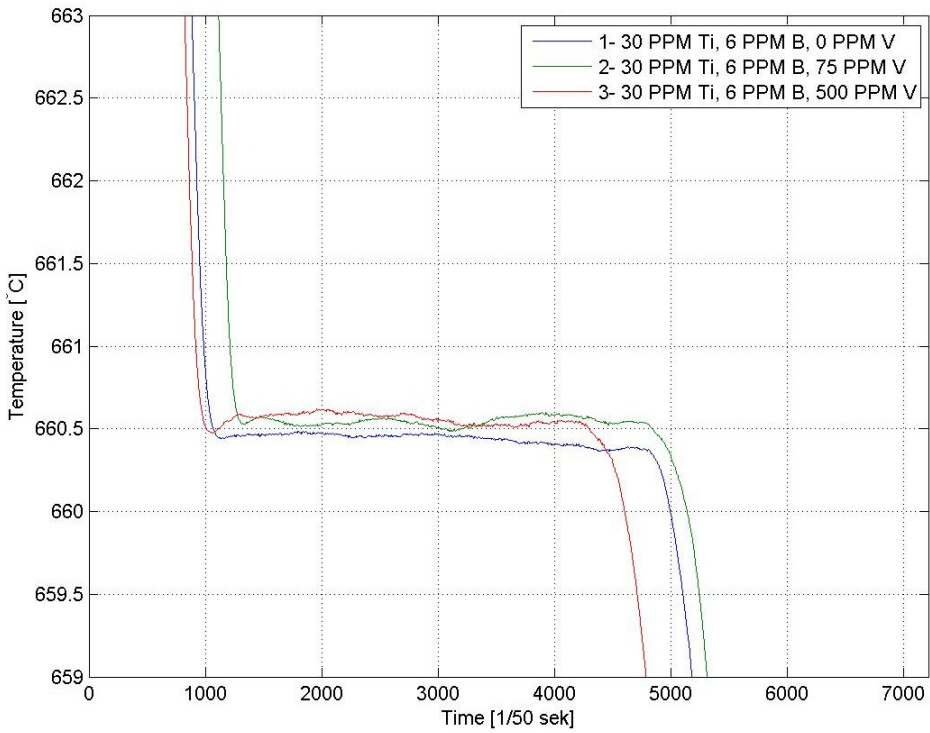
Figur 4.1: Average Temperature - Time curves from Thermal analysis of 5N alloy samples

The characteristic temperatures were extracted from the thermal analysis of each parallel samples before averaging over each compositions. The results are presented in **Table. 4.1**.

Tabell 4.1: Nucleation-, growth- and recalescence temperature from thermal analysis of 5N- alloy samples. The values were extracted from each thermal analysis before averaging.

	0 PPM V	75 PPM V	500 PPM V
T_n Nucleation Temperature	662.23	662.09	662.33
T_g Growth Temperature	660.54	660.60	660.64
T_m Minimum Temperature	660.41	660.49	660.45
ΔT_r Recalesence Temperature	0.13	0.11	0.19

4.1.2   Grain size

Representative images of the 3 5N- samples are displayed in **Fig. 4.2**.

Figur 4.2: The macro- etched structure of sample based on 5N-alloy. (Upper left) S-1, 0 PPM vanadium. (Upper right) 75 PPM vanadium. (Lower left) 500 PPM vanadium. (Lower right) Cross-section of S- 2 for view of the columnar grains from the crucible bottom. Red line indicates the height of the cut.
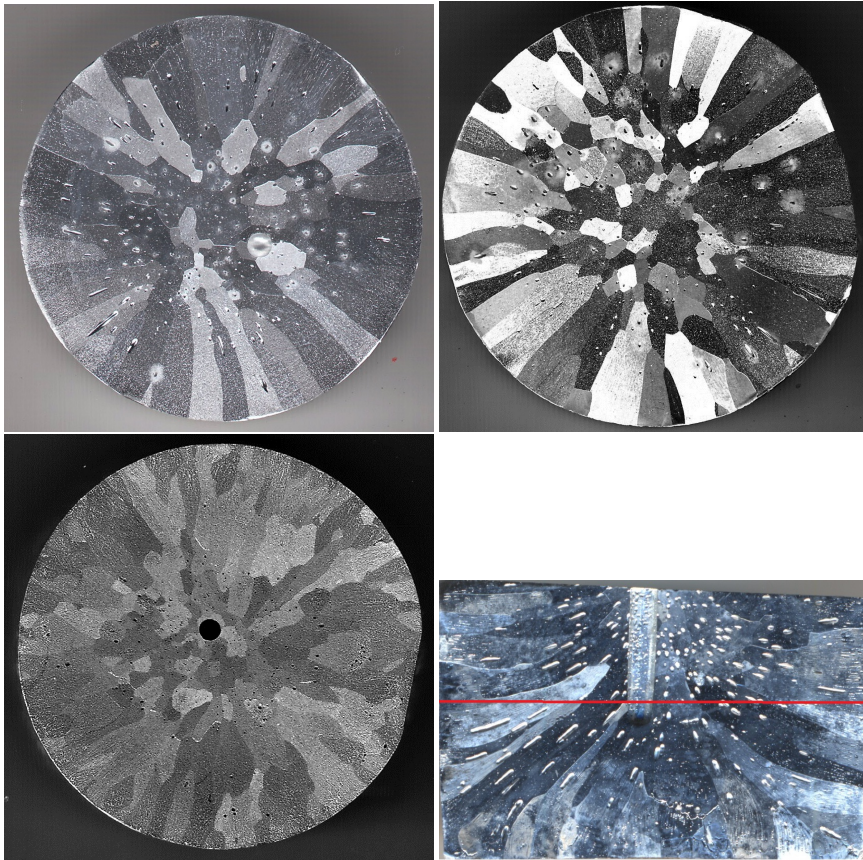
4.2 6060 Aluminium

4.2.1 Thermal Analysis of 6060- Alloy

The temperature - time curves measured were smoothed and average curves were constructed relative to point of maximum curvature (recalescence temperature). A high resolution part of the resulting curves for the different vanadium compositions is displayed in **Fig. 4.3**. The thermal couple drift check revealed large variations for one of the thermocouple after the first set. The two temperature- time curves constructed by this thermocouple were for that reason discarded and the remaining measurements were all conducted with the same thermocouple. The average curve for Sample CS-1 was hence constructed from only two measurements. The complete collection of thermal analysis is

provided in **Appendix. 7.8**.
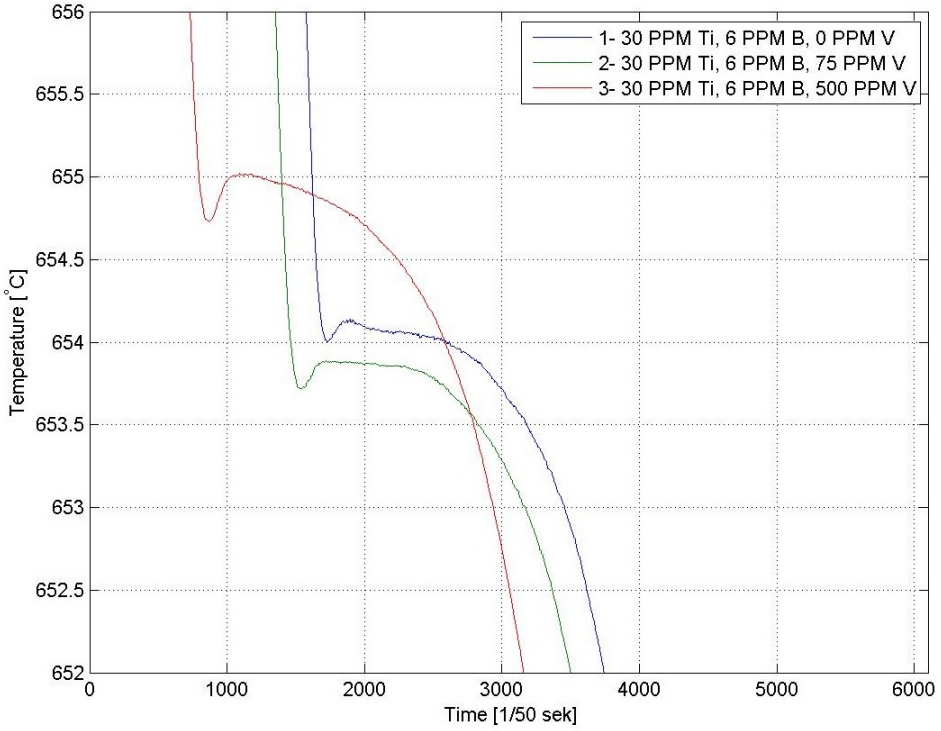
Figur 4.3: Average Temperature - Time curves from Thermal analysis of 6060- samples

The characteristic temperatures were extracted from the thermal analysis of each parallel samples before averaging over each compositions. The results are presented in **Table. 4.2**.

Tabell 4.2: Nucleation-, growth- and recalescence temperature from thermal analysis of 6060- samples. The values were extracted from each thermal analysis before averaging.

	0 PPM V	75 PPM V	500 PPM V
T_n Nucleation Temperature	655.83	655.63	656.20
T_g Growth Temperature	654.12	653.91	655.05
T_m Minimum Temperature	653.99	653.68	654.71
ΔT_r Recalesence Temperature	0.16	0.23	0.33

4.2.2 Grain Size Measurements

Representative pictures and grain size histograms based on mean lineal intercept method for the different samples are displayed in **Fig. 4.4-4.9**. The mean intercept length/ grain size for each sample is presented in **Table. 4.3**.

Figur 4.4: Microstructure (Left) and grain size histogram (Right) for sample CS- 1 (6060- Al, 0 PPM V, 30 PPM Ti, $1.25^{o}C/s$)

Figur 4.5: Microstructure (Left) and grain size histogram (Right) for sample CS- 2 (6060- Al, 75 PPM V, 30 PPM Ti, $1.25^{o}C/s$)
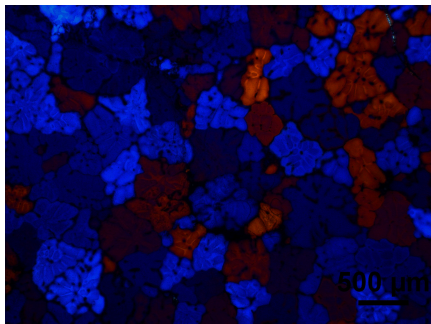
Figur 4.6: Microstructure (Left) and grain size histogram (Right) for sample CS- 3 (6060- Al, 500 PPM V, 30 PPM Ti, $1.25^{o}C/s$)
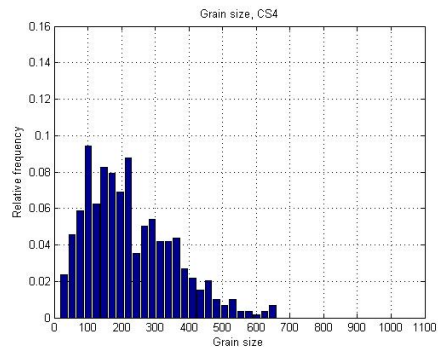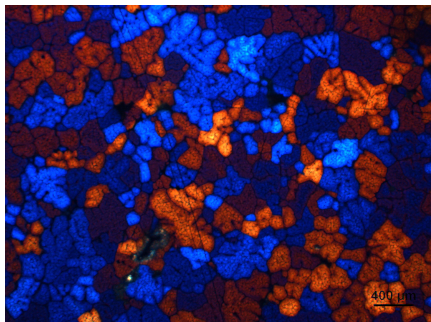
Figur 4.7: Microstructure (Left) and grain size histogram (Right) for sample CS- 4 (6060- Al, 0 PPM V, 60 PPM Ti, $1.25^{o}C/s$)
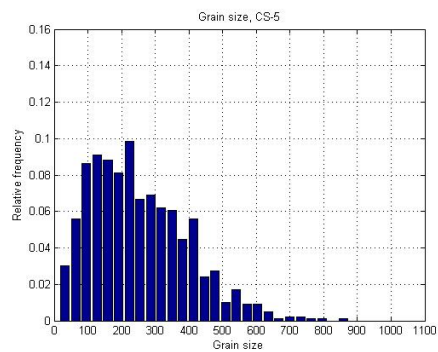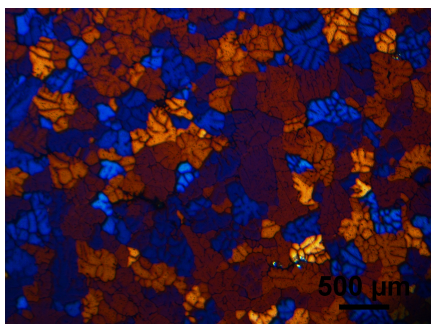
Figur 4.8: Microstructure (Left) and grain size histogram (Right) for sample CS-5 (6060- Al, 0 PPM V, 30 PPM Ti, $4.0^{o}C/s$)
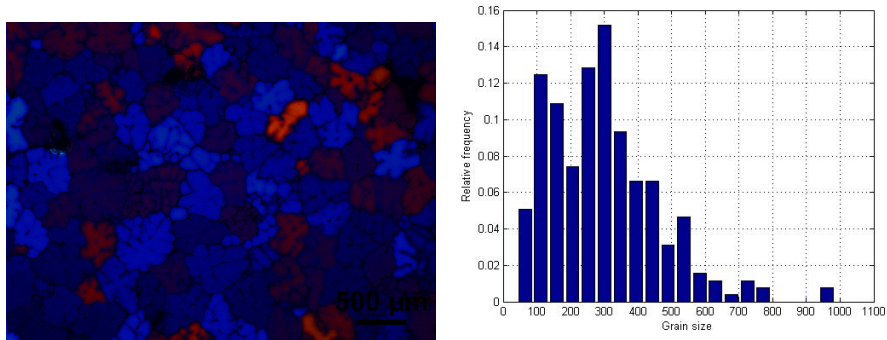
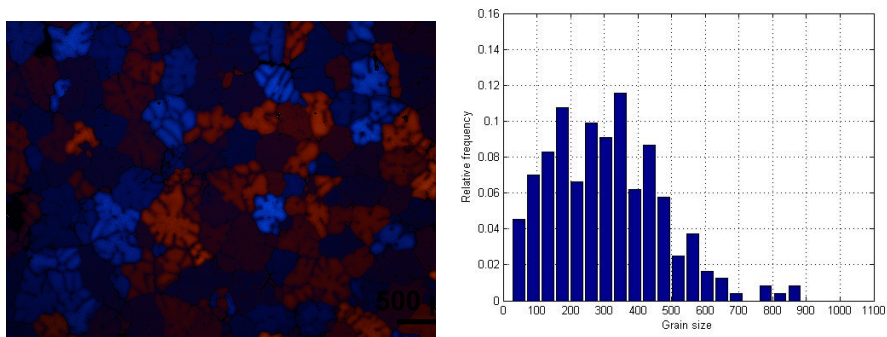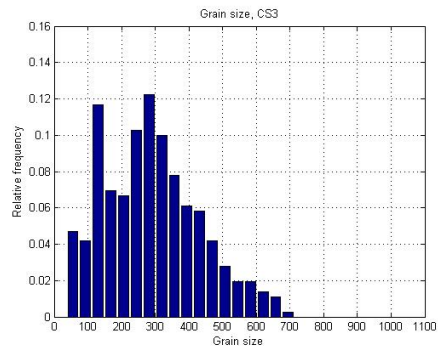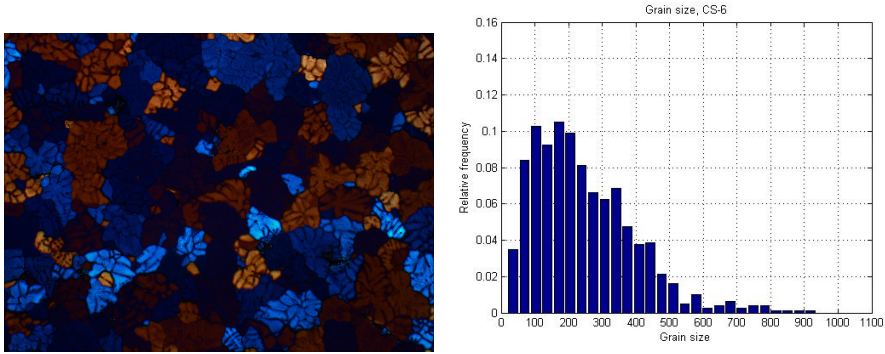**Figur 4.9:** Microstructure (Left) and grain size histogram (Right) for sample CS- 6 (6060- Al, 500 PPM V, 30 PPM Ti, $4.0^{o}C/s$)

Tabell 4.3: Median Grain size of 6060- samples based on results from mean intercept method.

	CS-1	CS-2	CS-3	CS-4	CS-5	CS-6
PPM V	0	75	500	0	0	500
PPM Ti	30	30	30	60	30	30
Cooling rate [^{o}C/s]	1.25	1.25	1.25	1.25	4.0	4.0
Grain size [μm]	299	311	283	225	254	244

4.3 Particle analysis

4.3.1 Edge- to- Edge Mismatch (E2EM)- Model

Based on the crystallographic data listed in **Table. 3.2**, the interatomic- and interplanar mismatch, f_r and f_d were calculated. **Fig. 4.10** and **Fig. 4.11** display the results for the complete assemble of closed- packed or near closed packed directions- and planes combinations.
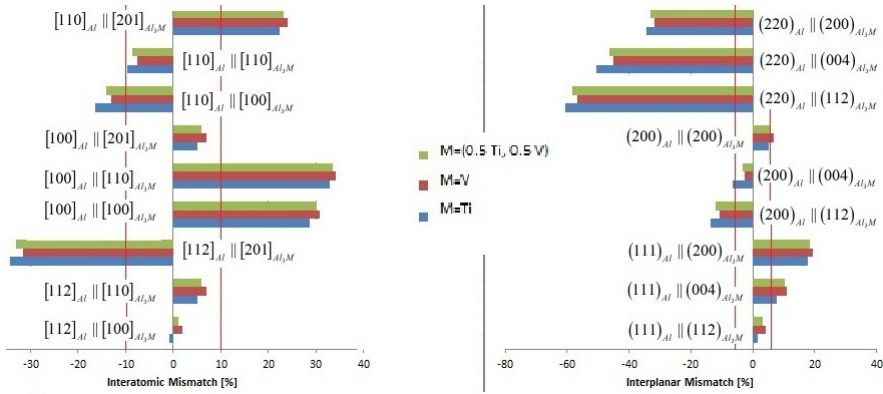
Figur 4.10: Calculated mismatch values for all closed- packed or near closed- packed directions and plane combinations for Al_3Ti, Al_3V and the mix; $Al_3(0.5Ti, 0.5V)$. A red line indicate the 10 % and 6 % threshold for interatomic and interplanar mismatch, respectively. Of these values, only a few qualify for orientation relationships.
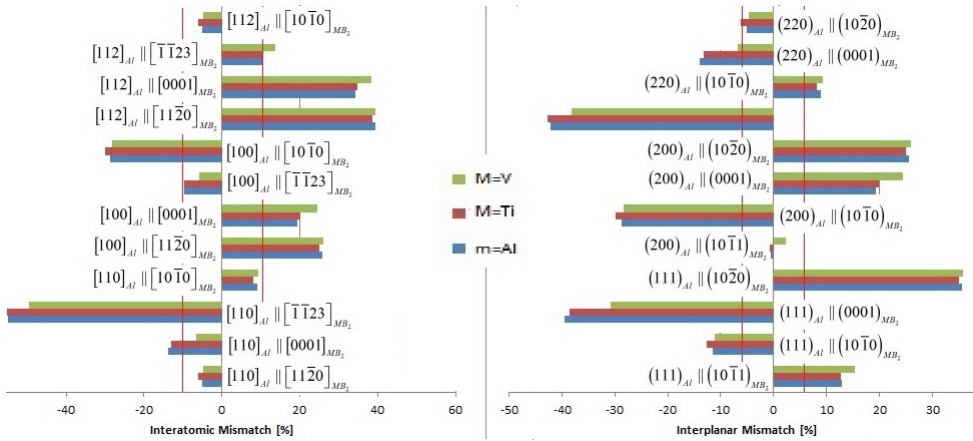
Figur 4.11: Calculated mismatch values for all closed- packed or near closed- packed directions and plane combinations for AlB_2, TiB_2 and VB_2. A red line indicate the 10 % and 6 % threshold for interatomic and interplanar mismatch, respectively. Of these values, only a few qualify for orientation relationships.

For orientation, one of two possible orientation relations for the diboride- α-Al interface is illustrated in **Fig. 4.12**.
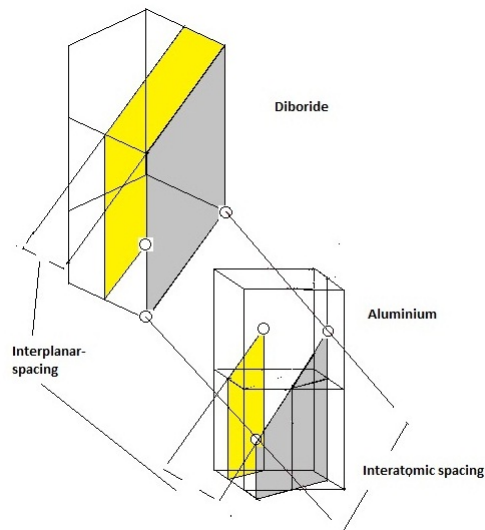
Figur 4.12: Illustration of MB_2 - α- Al orientation relationship

4.3.2 Scanning Electron Microscopy

EDS was used to identify titanium and boron in several particle clusters that were found at grain boundaries together with other particles. Such clusters was assumed to be TiB_2. **Fig. 4.13 and 4.14** show representative images and spectre of low and high vanadium samples. It is also included high resolution figures that emphasize the K- and L- peaks for both titanium and vanadium.
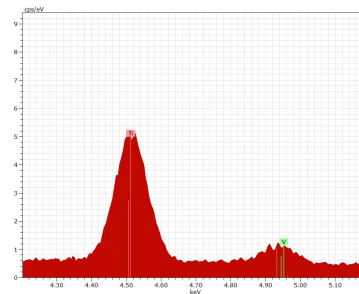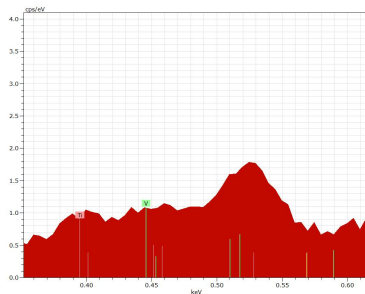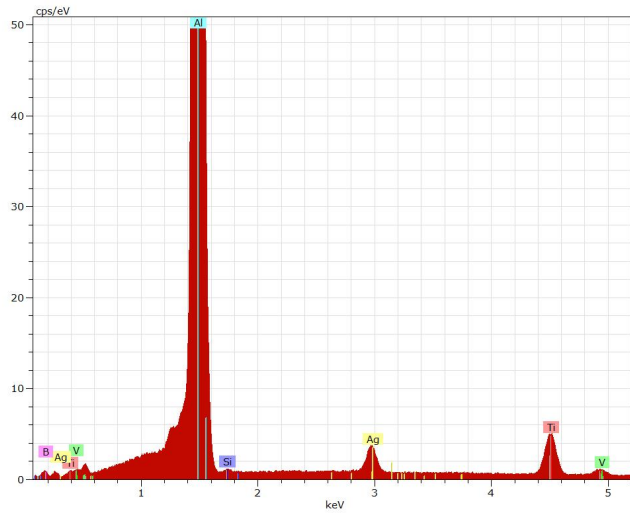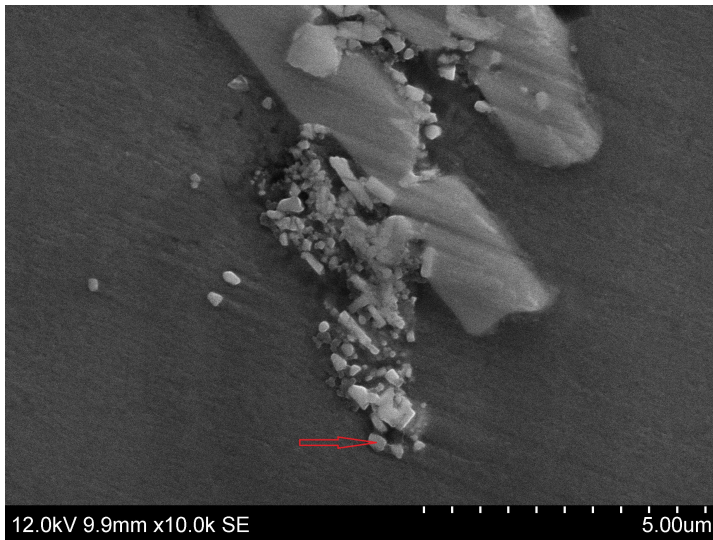
Figur 4.13: (Upper) Image of typical TiB_2- cluster found in a low vanadium sample. (Middle) Full EDS spectre from TiB_2. Location of interest indicated with red arrow. (Lower Left) Resolved part of the spectre covering the K- peaks of titanium and vanadium. (Lower Right) Resolved part of the spectre covering the L- peaks of titanium and vanadium.

l
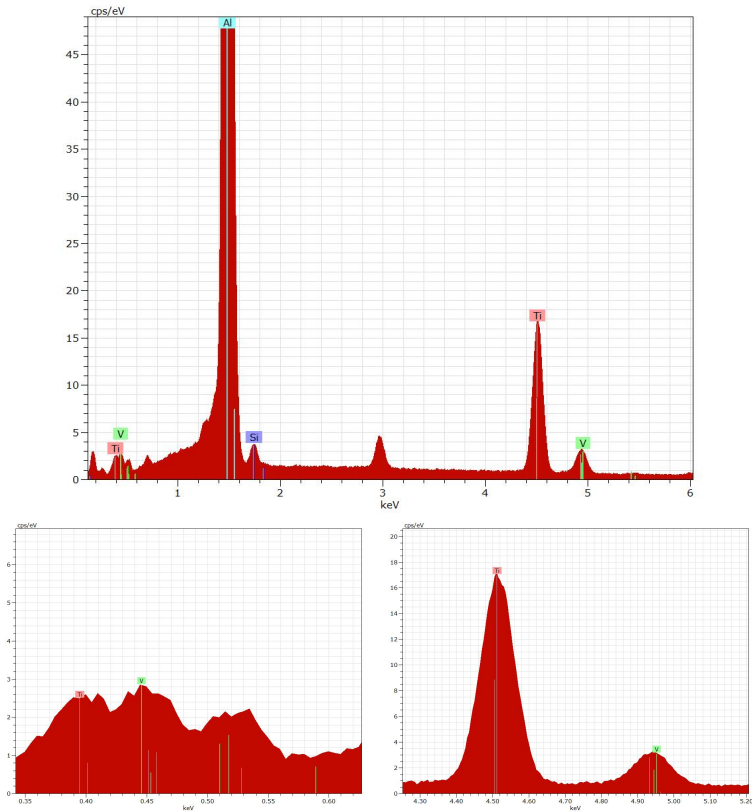
Figur 4.14: (Upper) Image of typical TiB_2- cluster found in a high vanadium sample. (Middle) Full EDS spectre from TiB_2. Location of interest indicated with red arrow. (Lower Left) Resolved part of the spectre covering the K- peaks of titanium and vanadium. (Lower Right) Resolved part of the spectre covering the L- peaks of titanium and vanadium.

4.3.3 Focus Ion Beam and Transmission Electron Microscopy

Focus Ion Beam was applied to extract and prepare a TEM- sample. The sample includes deboride particles. EDS was used to confirm the presence of titanium and boron in the particles. **Fig. 4.15** show pictures taken during the sample preparation. The TEM- sample was investigated in an Jeol TEM. Figure **Fig. 4.16** show a investigated particle.
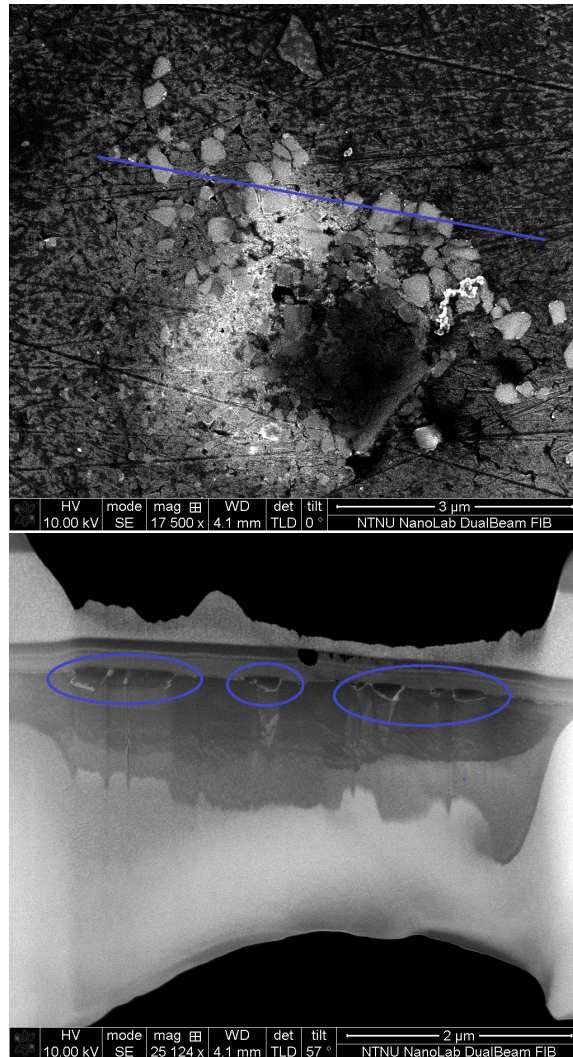
Figur 4.15: (Upper) diboride cluster at a grain boundary was extracted for investigation in TEM. Blue line mark the edge of the final cross- section. EDS was used to confirm titanium in the particles. (Lower) Final TEM- sample. A number of diboride particles were enclosed in the cross- section which can be investigated in TEM.
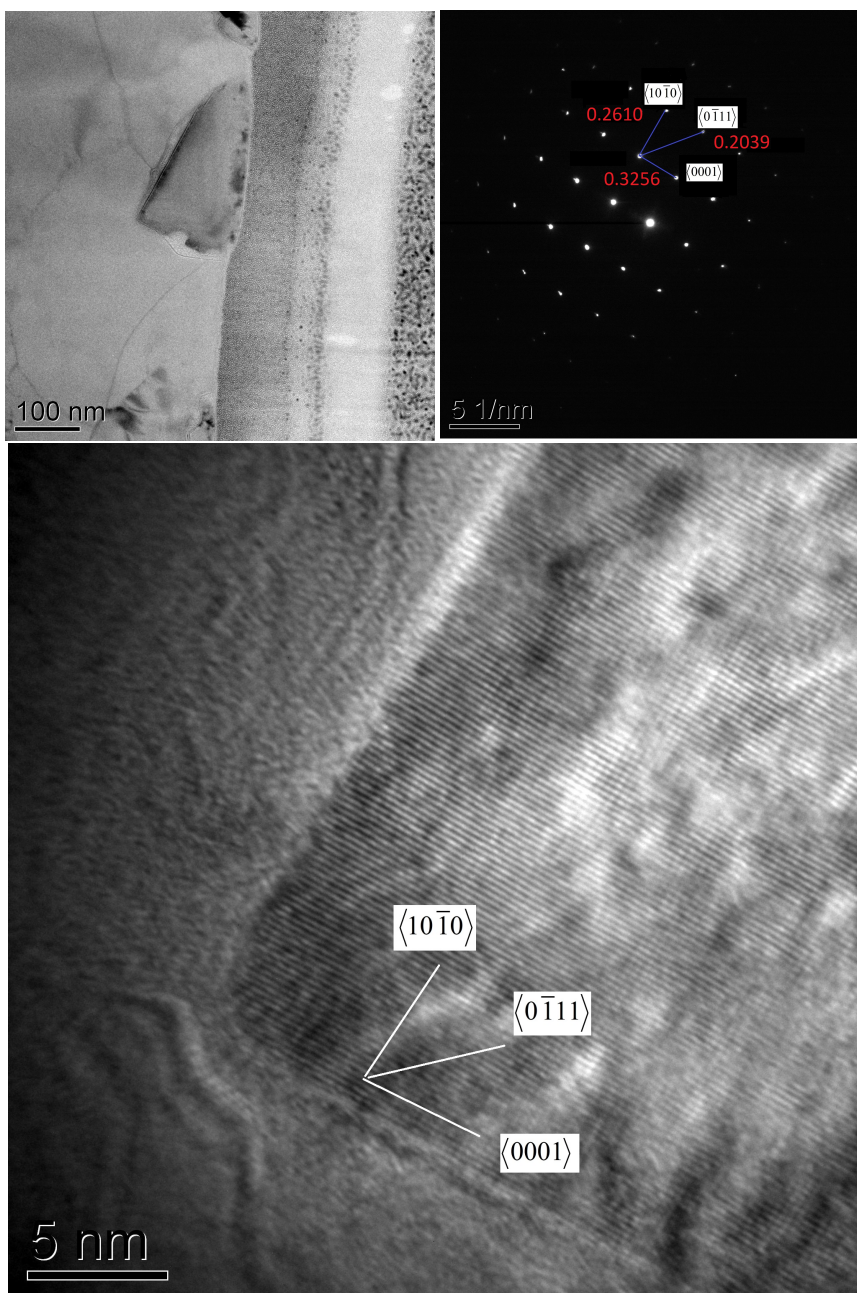
Figur 4.16: (Upper left) Overview of investigated particle. (Upper right) Diffraction pattern of the particle. Measured length spot distance indicated along three directions. (Lower) High resolution image of particle corner. The indicated crystal orientation is based on the diffraction pattern.

Two diborides were investigated by EDS in TEM. Both along the edge and in the centre of the particles. However, the obtained spectre did not vary with respect to vanadium. A representative spectre, which emphasizing vanadium is shown in **Fig. 4.17**.
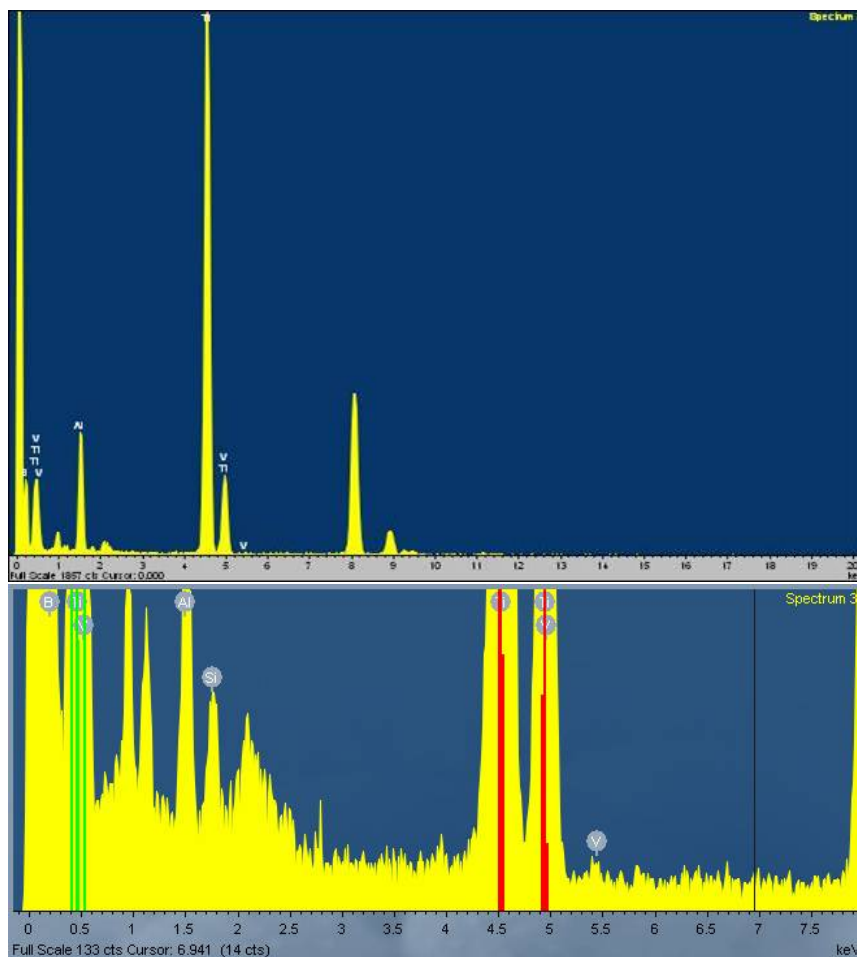
Figur 4.17: EDS Spectra obtained in TEM. The high voltage combined with a thin sample yield a nano- sized emission volume. The elements in the particle, not the surrounding matrix is resolved which increase the spectral resolution compared to EDS in SEM. (Upper) Full EDS spectra from the particle. The un- marked peaks are platinum, copper and gallium, which is from the sample preparation and sample holder. (Lower) Resolved portion of the above full spectra, which emphasizing the titanium and vanadium peaks.

Kapittel 5

Discussion

5.1 5N Aluminium

5.1.1 Thermal Analysis

The thermal analysis results covered in **Fig. 4.1** and **Table. 4.1** were constructed from the average temperature curves in **Appendix. 7.7**. The difference between the average curves for the different compositions (Fig. 4.1) and the characteristic temperatures **(Fig. 4.1)** is approximately 0.1- 0.2 ^{o}C. The reproducibility of the temperature curves and characteristic temperatures were in the range of $\pm$ 0.6 ^{o}C **(Appendix. 7.7)**. The uncertainty is hence too large too signify any difference between the different compositions. Growth temperature (T_g) measurements were slightly higher then the expected liquidus temperature of 660.3 ^{o}C. However, the differences were within uncertainty of the measurements. The nucleation temperature (T_n) were 1-2 ^{o}C higher than T_g. A T_n above the growth temperature is expected for a hyper- peritectic alloy, where the peritectic reaction starts at 665 ^{o}C. According to a peritectic phase diagram **(Fig. 2.8)**, no pre- liquidus reaction is expected for hypo- peritectic alloys. This should also have been the case for the conducted investigation. However, (Johnsson et al., 1993) found T_n for hypo- peritectic alloys to be higher than T_g (and higher than the liquidus temperature) for certain Al-Ti-B master alloys compositions **(Fig. 5.1)**. Higher- than- liquidus T_n were usually seen for Al-4.8Ti-Bt master alloys, similar to the master alloys used in the conducted investigation. A more recent investigation on a Al-Ti-B refined A356 Al- Si alloy also found T_n to be higher than T_g (Nafisi and Ghomashchi, 2006). However, this was arguable not the case for low master alloys additions (as in the conducted investigation) **(Fig. 5.1)**.
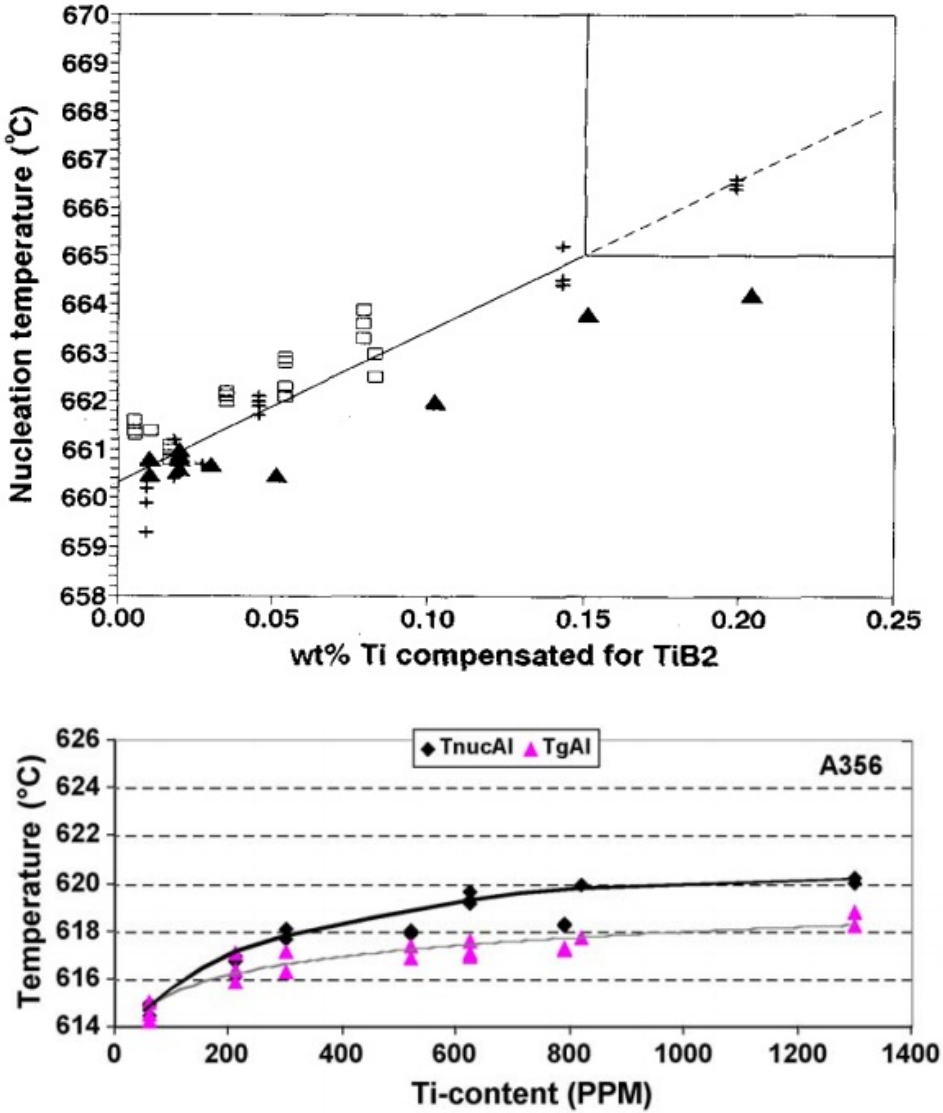
Figur 5.1: (Upper) Measured nucleation temperatures compared to the liquidus temperature at different Al-Ti-B master alloys additions. The liquidus line has been adjusted for the boron additions, which means that the liquidus temperature has decreased (Johnsson et al., 1993). (Lower) The change in T_n and T_g due to Al-Ti-B master alloys additions to a A356 Al- Si alloy (Nafisi and Ghomashchi, 2006).

The adsorption theory (Kim and Cantor, 1994) allocate Al_3Ti in hypo- peritectic systems, which can cause a T_n above the liquidus temperature. However, the Al_3Ti layer is only a few atom- layers thin which means that the total Al_3Ti volume is arguable too

small to cause a notable release of latent heat by a peritectic reaction. Whatever the case, the conducted investigation aimed to document potential changes in the characteristic temperatures due to vanadium. As mentioned above such changes could not be supported.

5.1.2 Grain size

Evidently from **Fig. 4.2** the microstructure for all 5N- samples were mainly columnar. **Fig. 4.2** show that the seemingly equiaxed zone in the middle are actually columnar grains extending from the bottom. This suggest that the grain refinement were not efficient enough to cause an columnar- to- equiaxed (CTE). Increased vanadium additions did arguable have an limited refining effect, as the high- vanadium samples had somewhat smaller columnar grains. Addition of vanadium is expected to increase the growth restriction factor- in other words increase the constitutional undercooling in front of the growing columns. This might be enough to develop enough undercooling to activate inoculants in front of the columns. However, without a fully equiaxed structure, the investigation was considered inconclusive.

5.2 6060 Aluminium

5.2.1 Thermal Analysis

The thermal analysis results covered in **Fig. 4.3** and **Table. 4.2** were constructed from the average temperature curves in **Appendix. 7.8**. The reproducibility of the temperature curves and characteristic temperatures were in the range of ± 0.4. T_n was also in this case measured higher than T_g. However, T_n was similar, but slightly higher than the results obtained for a commercial 6063- alloy by (Bäckerud et al., 1986). In contrast to the temperature curves from the investigation of the 5N- alloy, the thermal analysis of the 6060- Al based samples changed from composition to composition. A increase in T_n and T_g of 0.4 and $1\ ^oC$, respectively, were measured due to the 500 PPM vanadium addition. The aluminium rich part of the Al- V binary system has some upward liquidus slope with increasing vanadium additions **(Fig. 2.13)**. The upwards slope is expected to increase both T_n and T_g by 0.66 ^oC due to 500 PPM vanadium addition. However, such behaviour should have been more prevalent for the 5N-samples. The thermal analysis results of 5N- samples did not change by vanadium additions and were hence inconsistent with the thermal analysis of the 6060- alloy samples. The inconsistencies may be explained by the uncertainty associated with the measurements. The results may also bee explained by an systematic error for the measurements of either 5N- or 6060- 500 PPM samples. Daily variations in room temperature or unstable temperature along the data logger- thermocouple connection can cause misreadings.

5.2.2 Grain size

The micro structures were investigated and quantified by applying mean lineal intercept method to images taken under polarized light. Two different samples were investigated for each composition and the total number of interceptions were approximately 1000. The

results were hence considered reliable. The grain sizes were investigated thoroughly for two different cooling rates. Optical microscopy images did not indicate any systematic change in the grain size. The same could be seen from the histograms **(Fig. 4.4- 4.9)**, where the median grain sizes were approximately 300μm for all samples at a cooling rate of $1^oC/s$. For comparison, the limited addition of titanium for sample CS-4, had a significant larger refining effect than the increase in vanadium **(Fig. 4.7)**. At a cooling rate of $2.5^oC/s$, the median grain size decreased to approximately 230μm for both high- and low vanadium samples. From the results no correlation between the grain size and vanadium levels was found. This supports that an systematic error caused the variations obtained by thermal analysis.

5.3   SEM- investigation of diboride particles

Borides were investigated with respect to vanadium. The borides found were in clusters at the grain boundaries. This means that the borides found were not the ones responsible for inoculation, but particles pushed by the growing grains. However, the borides were formed, with or without vanadium, before solidification. This means that the grain boundary borides could be assumed to have the same composition as those responsible for nucleation. Distinct titanium peaks could be observed from the individual particles EDS- spectre. However, for both the L- and K- peaks, the β- titanium peak is located at very similar energy to that of the vanadium α- peak. To distinguish the two, the intensity ratio between the α- and β- peaks were evaluated. This ratio is characteristic for the elements so that any detected vanadium will contribute to the titanium β- peaks and alter the α/β- ratio. The EDS- software can rescale the α- peaks and indicate the intensity of the β- peaks. **Fig. 4.13 and 4.14** resolve the titanium and vanadium L- and K- peaks for both low and high vanadium addition samples. For the K- peaks, the intensity- noise ratio of the titanium and vanadium was far to low to distinguish the two. The L- peaks were on the other hand better. However, the L_α-L_β ratio did fit the expected intensity ratio with little or no increased titanium β intensity. This suggest that no vanadium was present in the borides. However, a considerable intensity of the aluminium peak indicated that the emission volume extended into the surrounding aluminium matrix. This would effectively decrease the relative vanadium intensity from the borides and in turn the detection limit. The presence of vanadium in borides could therefore not be confirmed or disproved from the obtained EDS- spectre.

5.4   FIB/TEM- investigation

FIB was successfully applied to fabricated a TEM sample. TEM was then used to investigate the same sample. The diffraction pattern confirmed that the particles were in fact hexagonal TiB_2 particles. EDS indicated little or no vanadium. The nano- sized emission volume of EDS in TEM exclude all elements from the matrix. Although some contaminations from the chamber and preparation is found (copper from the sample holder and gallium from the ion- sputtering), the intensity of the crystal elements itself should be considerable. Only a small peak was arguable due to the presence of vanadium **(Fig. 4.17)**.

However, quantification frequently yielded zero $wt\%$ vanadium. Due to the lack of vanadium, both along the edge and in the bulk, the crystal properties of TiB_2 were deemed unchanged in the presence of vanadium in the melt.

5.5 Edge- to- Edge (E2EM)- Model

E2EM- model indicated little overall change where inflicted due to substitution of titanium or aluminium with vanadium **(Fig. 4.10 and 4.11)**. Of the evaluated orientation relationships evaluated, only a few satisfy the thresholds criteria of 6 % and 10 % interatomic and interplanar mismatch, respectively. The possible orientation relationships with and without vanadium substitution is presented in **Table. 5.1**.

Tabell 5.1: Change in in interatomic and interplanar induced by vanadium substitution.

Al/	Orientation	Interatomic mismatch [%]				Interplanar mismatch [%]			
		Al	Ti	$Ti_{0.5}/V_{0.5}$	V	Al	Ti	$Ti_{0.5}/V_{0.5}$	V
Al_3M	$(111)_{Al}\|\|(112)_{Al_3M}$, $[1\bar{1}0]_{Al}\|\|[20\bar{1}]_{Al_3M}$	-	-0.88	1.18	2.02	-	1.66	3.11	4.05
	$(111)_{Al}\|\|(112)_{Al_3M}$, $[1\bar{1}0]_{Al}\|\|[\bar{1}10]_{Al_3M}$	-	5.06	5.93	6.94	-	1.66	3.11	4.05
	$(200)_{Al}\|\|(200)_{Al_3M}$, $[011]_{Al}\|\|[021]_{Al_3M}$	-	-0.88	1.18	2.02	-	5.06	5.90	6.94
	$(200)_{Al}\|\|(200)_{Al_3M}$, $[010]_{Al}\|\|[010]_{Al_3M}$	-	5.06	5.93	6.94	-	5.06	5.90	6.94
MB_2	$(200)_{Al}\|\|(10\bar{1}1)_{MB_2}$, $[011]_{Al}\|\|[1\bar{2}10]_{MB_2}$	-5.10	-6.11	-	-4.71	-0.57	-0.87	-	2.26
	$(220)_{Al}\|\|(11\bar{2}0)_{MB_2}$, $[\bar{1}12]_{Al}\|\|[1\bar{1}00]_{MB_2}$	-5.10	-6.11	-	-4.71	-5.10	-6.11	-	-4.71

5.6 Effect of vanadium on growth restriction

Vanadium was found to be a slow diffuser in aluminium (Murarka et al., 1968). The element is also associated with an steep liquidus slope, which forces segregation **(Table. 2.2)**. This results in considerable constitutional undercooling and associated high GRF in an binary Al- V system. The interaction between titanium and vanadium was found to be small (Kostov and Živković, 2008; Murray, 1981). Thus was the total GRF found by adding the individual GRFs for titanium and vanadium reasonable accurate (Easton and StJohn, 2001; Quested et al., 2005). The resulting GRF for the titanium and vanadium content found by GDMS **(Appendix. 7.5)** applied in this investigation is listed in **Table. 5.2**.

Tabell 5.2: Calculated GRFs for sample: S-1, S-2 ans S-3 based on GDMS- results. The total GRF was found by adding the individual GRFs. This is reasonable accurate due to little interaction between the titanium and vanadium elements. In addition was the alloy content low.

GRF	S-1	S-2	S-3
GRF (Si)	0.002	0.001	0.004
GRF (Ti)	0.59	0.63	0.79
GRF (V)	0.0003	0.15	0.92
GRF (Total)	0.59	0.78	1.71

Note that the real samples also hold other elements that is not accounted for in the calculated GRF- values. **Table. 5.2** indicates that vanadium could have a large impact in the grain size. This hold true for pure alloys, where an increase in GRF would have a notable effect. For commercial alloys, alloy elements and grain refiners introduce a significant GRF. Additional additions have little effect on the grain size- the GRF effect is saturated (Easton and StJohn, 2001). This corresponded with the results. Investigation of vanadium additions to a pure 5N- based alloys arguable indicated that the columnar grains breaks up earlier. For investigation on 6060- based alloys, no effect was be seen. Already introduced alloy elements and grain refiners have already induced a high GRF, and additional increase had little effect.

5.7 Effect on inoculation

As there was no observed effect of vanadium on the thermal analysis or microstructure, the inoculation performance was evidently unchanged. The potential effect could have been by substitution with aluminium and titanium in borides or with titanium in Al_3Ti. This could have altered the inoculation performance. However, E2EM- modelling indicated little change to the critical inoculants. Substitution of titanium or aluminium with vanadium in the borides improved the interatomic mismatch slightly. The interplanar mismatch decreased by 1% for $(220)_{Al}||(12\bar{2}0)_{MB_2}, [\bar{1}12]_{Al}||[1\bar{1}00]_{MB_2}$- oriental relationship, but increased with $2-3\%$ for $(200)_{Al}||(10\bar{1}1)_{MB_2}, [011]_{Al}||[1\bar{2}10]_{MB_2}$- oriental relationship. The interatomic mismatch was thought to be more important and the resulting effect was small and arguable positive for inoculation. For Al_3Ti, substitution of titanium with vanadium did increase the interatomic and interplanar mismatch with aluminium with approximately 1% and 2%, respectively. Also this were arguable too little to have much effect. Still, vanadium had a theoretical impact of crystal mismatch and the inoculation properties of both borides and Al_3Ti. Whether this effect was positive or negative would depend on the exact inoculation mechanism and the role of Al_3Ti. However, thermal analysis could not resolve any effect of vanadium that could be directly associated with the inoculation performance. Nor did the grain size respond in a manner that supported any effect of vanadium. It should be noted that although vanadium substitution did not change the inoculation properties, substitution with titanium will increase the titanium content in the melt. Excess titanium will in turn have an larger per- atom affect on growth restriction than vanadium **(Table. 2.2)**. However, no effect of vanadium on the final microstructure supported any direct or indirect effect of vanadium substitution. In addition could not EDS-

investigation of the borides support that substitution took place at all. This was confirmed by EDS in TEM.

Kapittel 6

Conclusion

Solidification experiments have been carried out with vanadium levels up to 500 ppm. Characterization methods, including thermal analysis, optical-, electron- microscopy and focused ion beam have been applied. The results from these experiments have lead to the following conclusions:

- Thermal analysis and investigation by optical microscopy do not support any effect of vanadium on grain refinement of aluminium alloys with the investigated compositions and parameters. This is consistent with the recent literature. Theoretical evaluations indicate that vanadium may have a limited grain refining effect both by a positive contribution to the growth restriction factor (GRF) and improved inoculant to α- Al crystal matching.

- Literature indicates that vanadium may have a measurable effect at hyper- peritectic additions.

- The amount of vanadium in borides at the grain boundaries are bellow the detection limit of EDS in both conventional SEM and TEM.

- Focused Ion Beam could successfully be used to extract inoculants for investigation TEM.

Kapittel 7

Future Work

The results from this thesis are consistent with the most recent literature on the theme. Vanadium has little or no effect on the grain refinement of aluminium and its alloys at low, hypo- peritectic levels. If any effect can be revealed, theoretical evaluations suggest that such effect would be positive with respect to grain refinement. Grain refinement experiments conducted with pure aluminium did not achieve columnar- to- equiaxed transition (CTE). CTE- transition is critical for investigation of grain refinement. Future work on pure- aluminium should maintain a CTE- transition, either by increased additions of grain refiners or increased crucible dimensions. It would also be relevant to apply standardized grain refinement tests. This can be TP-1, which simulates the conditions found for commercial DC- casting processes. Addition of titanium is a cost- issue and should be limited. Both VB_2 and Al_3V can prove efficient inoculants and vanadium itself hold a high growth restriction factor (GRF). Vanadium may therefore have potential to act as a supplement to titanium. In such case challenges are related to the stability of the particles at high temperature. Poisoning and substitution mechanisms should also be studied further. The complex hypotheses that explains the efficient inoculation of aluminium gives room for many potential ways elements can interfere- both alone and in combinations. Further work must strive to reveal the actual mechanisms that dictate grain refinement. This is necessary in order to efficiently utilize both alloy- elements and impurities to achieve the right microstructure and optimal properties. This thesis has also investigated the potential of application of focused- ion beam (FIB) for investigation of inoculant particles. Particles can easily be extracted for further investigation in transmission electron microscope (TEM) where the particles can be investigated in atomic scale. Such investigation has never been done before on a real alloy. Although this work only included investigation of excess borides, not responsible for the actual inoculation, investigation of the inoculant is in principle available.

Bibliografi

Abdel-Hamid, A. A. A., 1989. Effect of the refractory metals v, mo,zr and ta. Metallkd.

Arnberg, L., Backerud, L., Klang, H., 1982. Grain refinement of aluminium - 2. intermetallics particles in al-ti-b type master aalloys for grain refinement of aluminium. Metals Technology 9 (pt 1), 7–13.

Bäckerud, L., Krol, E., Tamminen, J., 1986. Solidification Characteristics of Aluminium Alloys Volume 1: Wrought Alloys. Skanaluminum.

Bäckerud, L., Yidong, S., 1991. Grain refining mechanisms in aluminium as a result of additions of titanium and boron. Aluminium.

Boulechfar, R., Meradji, H., S., G., Drablia, S., 2010. Investigation of $al_3ti_{0.5}v_{0.5}alloy$. Int. J. Nanoelectronics and Materials.

Bunn, A. M., Schumacher, P., Kearns, M. A., Boothroyd, C. B., Greer, A. L., 1999. Grain refinement by al-ti-b alloys in aluminium melts: a study of the mechanisms of poisoning by zirconium. Materials Science and Technology.

Cantor, B., 2003. Heterogeneous nucleation and adsorption. Philosophical Transactions of the Royal Society A: Mathematical, Physical and Engineering Sciences.

Chai, G., Bäckerud, L., Arnberg, L., 1995. Relation between grain size and coherency parameters in aluminium alloys. Materials Science and Technology (11), 1099–1103.

Choate, W. T., Green, A. A. S., 2004. Modeling the impact of secondary recovery (recycling) on u. s. aluminum supply and nominal energy requirements. Light Metals.

Cook, R., Kearns, M. A., Cooper, P. S., 1997. Effect of residual transition metal impureties on electrical conductivety and grain refinement of ec grade aluminium, and light metals. In: TMS.

Cooper, P. S., Kearns, M. A., 1996. Removal of transition metal impureties in aluminium melts by boron additives. Material Science Forum.

Dahle, A. K., Arnberg, L., 1997. On the assumption of an additive effect of solute elements in dendrite growth. Materials Science and Engineering: A.

Diplas, S., Tsakiropoulos, P., Shao, G., Watts, J. F., Matthew, J. A. D., 2002. A study of alloying behaviour in the ti-al-v system. Acta Materialia, 1951 – 1960.

Easton, M., StJohn, D., June 1999a. Grain refinement of aluminiim alloys: Part 2. confirmation of, and a mechanism for, the solute paradigm. Metallurgical and Materials Transactions A 30A, pages.

Easton, M., StJohn, D., June 1999b. Grain refinement of aluminium alloys: Part 1. the nucleant and solute paradigms - a review of litterature. Metallurgical and Materials Transactions A 30A, pages.

Easton, M. A., StJohn, D. J., 2001. The effect of alloy content on the grain refinement of aluminium. Light Metals.

Edwards, L., Backhouse, N., Darmstadt, H., Dion, M., 2012. Evolution of anode grade coke quality. Light Metals 2012.

Grandfield, J., Sweet, L., Davidson, C., Mitchell, J., Beer, A., Zhu, S., Chen, X., Easton, M., 2013. An initial assessement of the effect of increased ni and v content in a365 and aa6063 alloys. Light Metals 2013 (TMS).

Granger, D. A., 1998. Grain refining of aluminium and its alloys using inoculants. Light Metals, 941–952.

Greer, A. L., 2011. Metallurgical control of microstructure. 12th International Summer School- Vicenza.

Greer, A. L., Bunn, A. M., Tronche, A., Evans, P. V., Bristow, D. J., 2000. Modelling of inoculation of metallic melts: application to grain refinement of aluminium by al-ti-b. Acta Materialia 48 (11), 2823 – 2835.

Hayes, F. H., 1995. The al-ti-v (aluminum-titanium-vanadium) system. Journal of Phase Equilibria 16 (2), 163–176.

Hunt, J., 1984. Steady state columnar and equiaxed growth of dendrites and eutectic. Materials Science and Engineering (65), 75–8l2,.

Jha, G., Ningileri, S., Li, X., Bowers, R., 2013. The Challenge of Effectively Utilizing Trace Elements/Impurities in a Varying Raw Materials Market. John Wiley and Sons, Inc., pp. 929–934.

Johnsson, M., Backerud, L., Sigworth, G. K., 1993. Study of the mechanism of grain refinement of aluminum after additions of ti- and b-containing master alloys. Metallurgical Transactions A.

Jones, G. P., 1985. The mechanism of nucleation of liquid aluminium by al-ti-b alloys. Int. Seminar Trondheim Norway.

Kashyap, K. T., Chandrashekar, T., August 2001. Effects and mechanisms of grain refinement in aluminium alloys. Bull. Mater. Sci 24 (4), 345–353.

Khaliq, A., Rhamdhani, M. A., Brooks, G. A., Grandfield, J., 2011. Thermodynamic analysis of ti, zr, v and cr imupities in aluminium melt. Light Metals.

Kim, W. T., Cantor, B., 1994. An adsorption model of the heterogeneous nucleation of solidification. Acta Metallurgica et Materialia.

Kostov, A., Živković, D., 2008. Thermodynamic analysis of alloys ti-al, ti-v, al-v and ti-al-v. Journal of Alloys and Compounds 460 (1-2), 164 – 171.

Kurz, W., 1998. Fundamentals of solidification. Trans Tech Publications.

Mahasneh, A. A., Al-Qawabah, S. M. A., 2011. Effect of vanadium addition at a rate of 0.1microhardness of al-cu casted alloys. Online Computer File 5, 92–102.

McCartney, D. G., 1989a. Grain refinement of aluminium and its alloys using inoculants. International Material Review.

McCartney, D. G., 1989b. Grain refining of aluminium and its alloys using inoculants. International Materials Review 34, 247–260.

Meltzman, H., Mordehai, D., Kaplan, W. D., 2012. Solid–solid interface reconstruction at equilibrated ni–al2o3 interfaces. Acta Materialia.

Mondolfo, L. F., 1976. Aluminum Alloys: Structure and properties. Butterworths.

Murarka, S. P., Anand, M. S., Agarwala, R. P., 1968. Diffusion of vanadium in aluminium and nickel. Acta Metallurgica.

Murray, J. L., 1981. The ti-v (titanium-vanadium) system. Bulletin of Alloy Phase Diagrams 2 (1), 48–55.

Murray, J. L., 1989. Al- v (aluminium- vanadium). Bulletin of Alloy Phase Diagrams.

Nafisi, S., Ghomashchi, R., 2006. Grain refining of conventional and semi-solid a356 al–si alloy. Journal of Materials Processing Technology.

Niels Hansen, N., 1977. The effect of grain size and strain on the tensile flow stess of aluminium at room temperature. Acta Metallurgica.

Predel, B., 1992. B- v (boron- vanadium). Landholt- Börnstein.

Qian, M., Cao, P., Easton, M. A., McDonald, S. D., StJohn, D. H., 2010. An analytical model for constitutional supercooling-driven grain formation and grain size prediction. Acta Materialia.

Qiu, D., Taylor, J., Zhang, M.-X., 2010. Understanding the co-poisoning effect of zr and ti on the grain refinement of cast aluminum alloys. Metallurgical and Materials Transactions A: Physical Metallurgy and Materials Science 41 (13), 3412–3421.

Quested, T., Dinsdale, A., Greer, A., 2006. Grain refinement of aluminium alloys: Thermodynamic analysis of poisoning by silicon. Mater. Sci. Technol.

Quested, T. E., Dinsdale, A. T., Greer, A. L., 2005. Thermodynamic modelling of growth-restriction effects in aluminium alloys. Acta Materialia 53 (5), 1323 – 1334.

Quested, T. E., Greer, A. L., 2003. Growth-restriction effects in grain refinement of aluminium. LIGHT METALS, 945–952.

Quested, T. E., Greer, A. L., 2004. The effect of the size distribution of inoculant particles on as-cast grain size in aluminium alloys. Acta Materialia 52 (13), 3859 – 3868.

Rappaz, M., Thévoz, P., 1987. Steady state columnar and equiaxed growth of dendrites and eutectic. Materials Science and Engineering (65), 1487–1497.

Rooy, E. R., 1989. Grain refining of aluminium and its alloys using inoculants. Metals Handbook 15, 743–770.

Schumacher, P., Greer, A. L., 1995. Study of the action of grain refining particles in aluminium alloys. TMS Light Metals.

Scumacher, P. S., Greer, A. L., 1994. Heterogenious nucleated α-al in amorphous aluminium alloys. Material Science and Engineering.

Wang, C. Y., Beckmann, C., 1994. Prediction of columnar to equiaxed transition during diffusion-controlled dendritic alloy solidification. Metallurgical and Materials Transactions A.

Wang, F., Liu, Z., Qiu, D., Taylor, J. A., Easton, M. A., Zhang, M. X., 2013. Revisiting the role of peritectics in grain refinement of al alloys. Acta Materialia.

Wang, T., Z., C., Fu, H., Gao, L., Li, T., 2012a. Grain refinement mechanism of pure aluminum by inoculation with al-b master alloys. Material Science and Enginering: A 549, 136–143.

Wang, X., Cong, F., Zhu, Q., Cui, J., 2012b. Effect of trace element vanadium on superplasticity of 5083 aluminium alloy sheets. Science China Technological Sciences 55, 510–514.

Zhang, M. X., Kelly, P. M., Easton, M. A., Taylor, J. A., 2005. Crystallographic study of grain refinement in aluminum alloys using the edge-to-edge matching model. Acta Materialia 53 (5), 1427 – 1438.

Zupanic, F., 2008. Composition and morphology of diborides in al-ti-b alloys after annealing at 1873 k. RMZ – Materials and Geoenvironment.

Appendix

7.1 5N- Al documentation

07.10.2004

GDMS-Analysis

Sample Identification: T1640

Grade: Al5N

Ag	< 5	ppb	Mg	1,41	ppm
As	11	ppb	Mn	47	ppb
B	58	ppb	Mo	< 5	ppb
Ba	< 5	ppb	Na	12	ppb
Be	< 5	ppb	Ni	< 5	ppb
Bi	< 5	ppb	O	< 10,0	ppm
Ca	< 20	ppb	P	526	ppb
Ce	782	ppb	Pb	< 5	ppb
Cl	< 100	ppb	Pd	< 100	ppb
Co	< 5	ppb	Pt	< 100	ppb
Cr	11	ppb	S	< 100	ppb
Cs	< 10	ppb	Sb	< 5	ppb
Cu	2,60	ppm	Si	869	ppb
F	< 100	ppb	Sn	< 50	ppb
Fe	504	ppb	Ti	65	ppb
Ga	< 5	ppb	Th	64	ppb
Ge	< 40	ppb	U	12	ppb
In	< 5	ppb	V	43	ppb
K	< 100	ppb	W	< 25	ppb
La	526	ppb	Zn	< 50	ppb
Li	< 5	ppb	Zr	8	ppb
Cd	< 50	ppb	Nd	148	ppb

7.2 6060- Al documentation

Si	Fe	Cu	Mn	Mg	Cr	Ni	Zn	Ti	V	Pb
0.4653	0.2	0.0002	0.01	0.3833	0.0006	0.0008	0.0038	0.0064	0.003	3.00E-04

Sn	B	Be	Na	Ca	Zr	Li	Sr	Sb	P	Ga
0	1.00E-04	1.00E-05	0.0011	3.00E-04	8.00E-04	1.00E-05	1.00E-04	3.00E-05	2.00E-04	1.11E-02

7.3 Al-5Ti-1B rod documentation

KBM MASTER ALLOYS

PACKING LIST /
ANALYSISREPORT
58228 / 1

KBM Master Alloys B.V.
P.O. Box 156, 9930 AD Delfzijl
Kloosterlaan 2, 9936 TE Delfzijl
The Netherlands
Telephone 0596-641911
Telefax 0596-617321

ALCOA NORWAY ANS
LUNDEVAEGEN
N-4550 FARSUND

PACKING LIST / ANALYSIS REPORT   8 December 2011

Your Order No. : 1008568-2.0/1
Our Order No.   : 58228 / 1
Product   : 5% TITANIUM 1% BORON BALANCE ALUMINIUM MASTER ALLOY IN THE
                  FORM OF ROD, DIA 9,5 MM, IN LENGTHS OF 100 CM.
                  COLOUR CODE - GREEN B.T.N. 760521000

Qty Ordered   :   3.375 KG
Qty Delivered   :   3.375 KG
Gross Weight   :   3.455 KG
Packing   :   4 Pallets

Pallet Number	Nett Weight In KG	Lot Heat Number	TI	B	SI	FE	V
K28674	1.000	K28674	4,8	1,0	0,10	0,10	0,02
K28675	1.000	K28675	4,8	0,9	0,10	0,10	0,02
K28676	1.000	K28676	4,9	1,0	0,10	0,08	0,02
K28677	375	K28677	4,8	1,0	0,10	0,08	0,02

WE CERTIFY THAT THE ANALYSIS ARE ACCURATE WITHIN
COMMERCIAL LIMITS

Q.C. DEPARTMENT

MC

Chamber of Commerce Groningen
reg. no. 02325066

Sales by / Verkauf durch / Vente par / Verkoop door:

Figur 7.1: Al- 5Ti- B master alloy rod documentation

7.4 OES

**Tabell 7.1:** Optical Emission Spectroscopy (OES) results of 6060- based samples

	AL	SI	FE	CU	MN	MG	CR	NI	ZN	TI	V	PB	SN	B
CS-1	98,78493	0,52910	0,19127	0,00016	0,00256	0,46262	0,00052	0,00121	0,00410	0,00629	0,00343	0,00026	0,00004	0,00071
CS-2	98,80193	0,51772	0,18899	0,00016	0,00257	0,45325	0,00056	0,00116	0,00379	0,00686	0,00872	0,00026	0,00005	0,00114
CS-3	98,85609	0,47967	0,17475	0,00018	0,00234	0,41660	0,00065	0,00111	0,00368	0,00616	0,04589	0,00022	0,00004	0,00077
CS-4	98,78146	0,53297	0,19352	0,00016	0,00259	0,45894	0,00052	0,00120	0,00405	0,00720	0,00331	0,00028	0,00004	0,00086
CS-5	98,84079	0,48909	0,17779	0,00019	0,00226	0,42165	0,00062	0,00107	0,00313	0,00553	0,04521	0,00022	0,00004	0,00075
CS-6	98,72879	0,55301	0,20504	0,00018	0,00259	0,48164	0,00051	0,00123	0,00351	0,00563	0,00320	0,00039	0,00012	0,00077

	BE	NA	LI	CA	ZR	GA	CD	BI	P	SB	SR	_V	_P	_T
CS-1	0,00000	0,00005	0,00000	0,00028	0,00086	0,01101	0,00005	0,00000	0,00033	0,00000	0,00010	0,01110	0,99172	0,02022
CS-2	0,00000	0,00019	0,00000	0,00036	0,00085	0,01085	0,00001	0,00001	0,00037	0,00000	0,00010	0,01700	0,97096	0,02083
CS-3	0,00000	0,00025	0,00000	0,00033	0,00078	0,00992	0,00001	0,00000	0,00035	0,00000	0,00010	0,05348	0,89627	0,01916
CS-4	0,00000	0,00009	0,00000	0,00030	0,00085	0,01105	0,00004	0,00000	0,00035	0,00000	0,00010	0,01188	0,99191	0,02148
CS-5	0,00000	0,00000	0,00000	0,00017	0,00072	0,01038	0,00002	0,00000	0,00016	0,00004	0,00010	0,05208	0,91074	0,01852
CS-6	0,00000	0,00000	0,00000	0,00023	0,00078	0,01187	0,00007	0,00003	0,00019	0,00000	0,00011	0,01013	1,03465	0,02023

7.5 GDMS

**Tabell 7.2:** Glow Discard Mass Spectroscopy (GDMS) results of 5N- based samples

Sample	S-1	S-2	S3
B	4.67 PPM	5.36 PPM	6.62 PPM
Si	3.76 PPM	2.37 PPM	6.38 PPM
Ti	25.3 PPM	26.9 PPM	33.7 PPM
V	0.1 PPM	51.3 PPM	307 PPM

7.6 Cooling rates
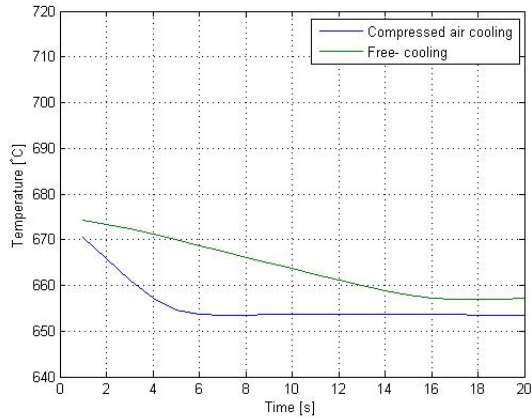
Figur 7.2: Measured cooling rates for the two different set- ups. Free- cooling gives a cooling rate of approximately 1.25 $^{o}C/s$, while compressed air cooling gives a cooling rate of approximately 4.0 $^{o}C/s$
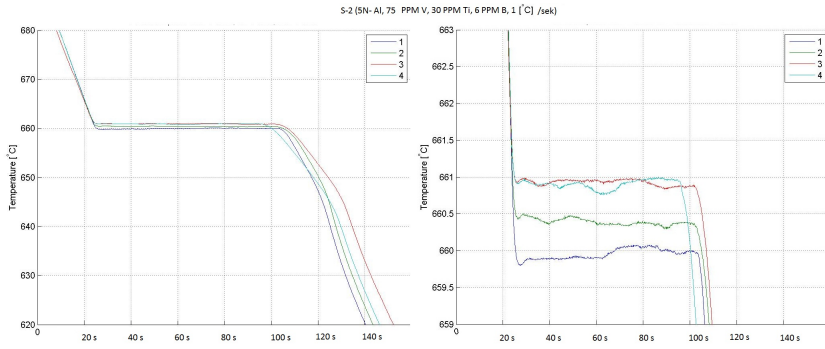
7.7 Thermal analysis, 5N- samples
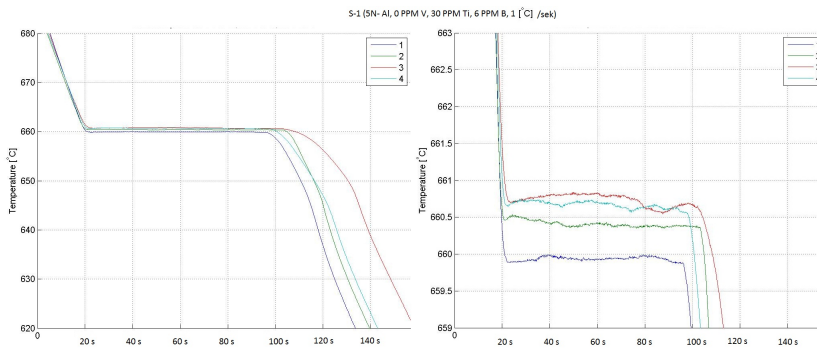
Figur 7.3: Thermal analysis results for S-1 (5N- Al, 0 PPM V, 30 PPM Ti, 6 PPM B, 1.25^{o}C/s).

Figur 7.4: Thermal analysis results for S-2 (5N- Al, 75 PPM V, 30 PPM Ti, 6 PPM B, 1.25^oC/s).
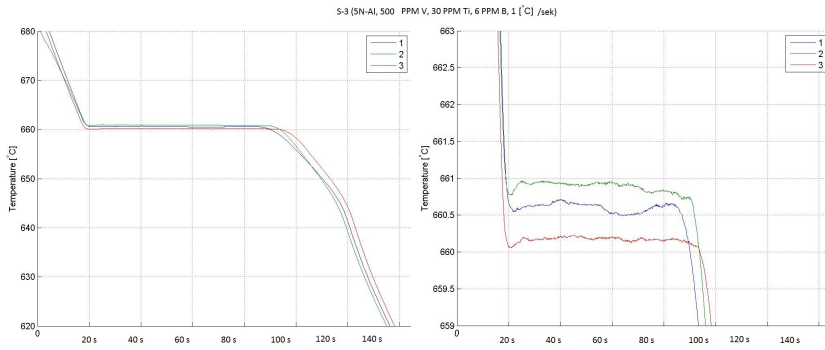
Figur 7.5: Thermal analysis results for S-3 (5N- Al, 500 PPM V, 30 PPM Ti, 6 PPM B, 1.25^oC/s).
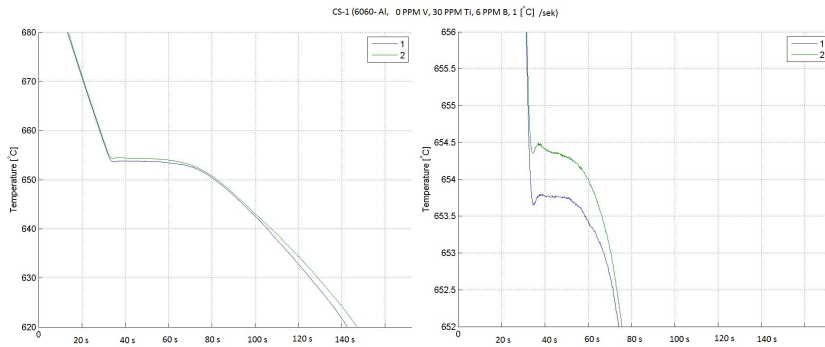
7.8   Thermal analysis, 6060- samples

Figur 7.6: Thermal analysis results for CS-1 (6060- Al, 0 PPM V, 30 PPM Ti, 6 PPM B, 1.25^oC/s).
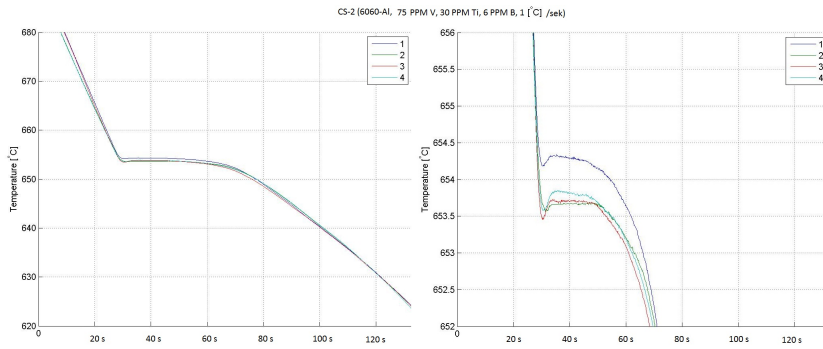
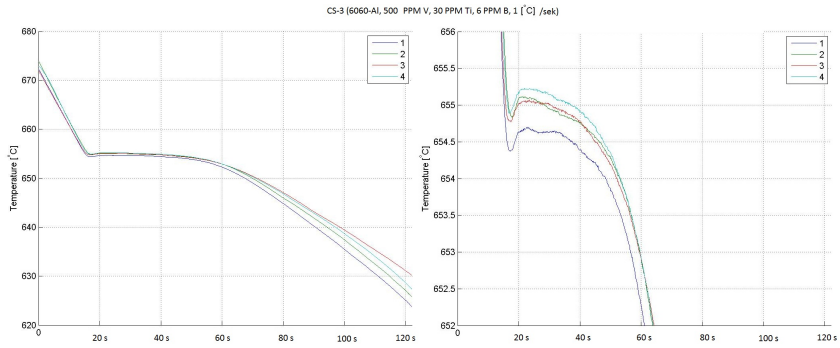**Figur 7.7:** Thermal analysis results for CS-2 (6060- Al, 75 PPM V, 30 PPM Ti, 6 PPM B, $1.25^{o}C$/s).

Figur 7.8: Thermal analysis results for CS-3 (6060- Al, 500 PPM V, 30 PPM Ti, 6 PPM B, $1.25^{o}C$/s).